

A multilayer model for thermal infrared emission of Saturn's rings. III: Thermal inertia inferred from Cassini CIRS

Ryuji Morishima^{1,2,3}, Linda Spilker², Keiji Ohtsuki^{3,4}

Ryuji.Morishima@jpl.nasa.gov

1: University of California, Los Angeles, Institute of Geophysics and Planetary Physics, Los Angeles, CA 90095, USA

2: Jet Propulsion Laboratory/California Institute of Technology, Pasadena, CA 91109, USA

3: Laboratory for Atmospheric and Space Physics, University of Colorado, Boulder, CO 80309, USA

4: Department of Earth and Planetary Sciences and Center for Planetary Science, Kobe University, 657-8501, Japan

Icarus 215, 107–127

Manuscript total pages: 47

Table: 7

Figures: 13

Proposed Running Head:

Thermal inertia of Saturn's ring particles

Editorial correspondence to:

Ryuji Morishima

Jet Propulsion Laboratory

M/S 230-205, 4800 Oak Grove Drive

Pasadena, CA 91109 Duane Physics - 392 UCB

Phone: +1 818 393 1014; Fax: +1 818 393 4495

e-mail: Ryuji.Morishima@jpl.nasa.gov

ABSTRACT

The thermal inertia values of Saturn’s main rings (the A, B, and C rings and the Cassini division) are derived by applying our thermal model to azimuthally scanned spectra taken by the Cassini Composite Infrared Spectrometer (CIRS). Model fits show the thermal inertia of ring particles to be 16, 13, 20, and 11 $\text{Jm}^{-2}\text{K}^{-1}\text{s}^{-1/2}$ for the A, B, and C rings, and the Cassini division, respectively. However, there are systematic deviations between modeled and observed temperatures in Saturn’s shadow depending on solar phase angle, and these deviations indicate that the apparent thermal inertia increases with solar phase angle. This dependence is likely to be explained if large slowly spinning particles have lower thermal inertia values than those for small fast spinning particles because the thermal emission of slow rotators is relatively stronger than that of fast rotators at low phase and vice versa. Additional parameter fits, which assume that slow and fast rotators have different thermal inertia values, show the derived thermal inertia values of slow (fast) rotators to be 8 (77), 8 (27), 9 (34), 5 (55) $\text{Jm}^{-2}\text{K}^{-1}\text{s}^{-1/2}$ for the A, B, and C rings, and the Cassini division, respectively. The values for fast rotators are still much smaller than those for solid ice with no porosity. Thus, fast rotators are likely to have surface regolith layers, but these may not be as fluffy as those for slow rotators, probably because the capability of holding regolith particles is limited for fast rotators due to the strong centrifugal force on surfaces of fast rotators. Other additional parameter fits, in which radii of fast rotators are varied, indicate that particles less than ~ 1 cm should not occupy more than a half of the cross section for the A, B, and C rings.

Key words: Saturn, Rings; Infrared observations; Radiative transfer, Regoliths

1. Introduction

This is our third paper analyzing thermal infrared data of Saturn’s rings. In Morishima et al. (2009; hereafter Paper I), we introduced our new multilayer model, and applied it to ground-based data obtained before the Cassini mission. In Morishima et al. (2010; hereafter Paper II), we improved our code, and estimated the values of the albedo and the ratio of fast and slow rotators using thermal data radially scanned by the Cassini Composite Infrared Spectrometer (CIRS). In the present paper, we estimate the thermal inertia values of Saturn’s rings using thermal data azimuthally scanned by Cassini CIRS including those in Saturn’s shadow.

Saturn’s main rings (the A, B, and C rings and the Cassini division) consist of a numerous number of icy particles. The range of the particle size deduced from radio and stellar light occultations is roughly 1 cm to 10 m (Marouf et al., 1983; Zebker et al., 1985; French and Nicholson, 2000; Cuzzi et al., 2009). The ring spectra in ultra-violet (Bradley et al., 2010), near-infrared (Poulet et al., 2003; Nicholson et al., 2008), and far-infrared (Spilker et al., 2005) light indicate that surfaces of ring particles are covered by tiny regolith particles ranging from

micron to cm sizes.¹ This means that the largest regolith particles are comparable to the smallest free floating ring particles. The abundance of free floating micron-size grains is likely to be negligible (Dones et al., 1993), except when spokes form (e.g., D’Aversa et al., 2010). Most likely, most of small grains (< cm) stick to larger particles due to the surface energy (e.g., Choksi et al., 1993). The composition of ring (or regolith) particles is mostly crystalline water ice and the mass fraction of contaminants (Tholins, PAHs, or nanohematite) is less than a percent (Poulet et al., 2003; Cuzzi et al., 2009).

Besides the spectroscopy, thermal infrared observations can provide unique information about the surface layers of icy particles and about the particle size. The ring temperature drops during particles pass through Saturn’s shadow and increases after they exit from the shadow to the sunshine. The degree of the temperature drop increases with decreasing thermal inertia of the particle, if the particle size is larger than the thermal skin depth for eclipse. The thermal inertia, which is given by the square root of the product of the physical density, the specific heat, and the thermal conductivity, represents how much the particle suppresses its temperature change against illumination flux change. While the uncertainties in the density and the specific heat may be only by a factor of 2-3, the thermal conductivity varies over several orders of magnitude depending on structures of surface layers. A numerical model of Shoshany et al. (2002) showed that the thermal conductivity decreases by a factor of 10^4 with increasing porosity from 0 to $\sim 80\%$. There has been no direct estimation of the porosity of ring particles. However, the internal density of ring particles of $\sim 450 \text{ kg m}^{-3}$ or less is favorable in dynamical simulations for formation of wakes in the A and B rings (Salo et al., 2001; Stuart et al., 2010), because signatures of wakes become too strong in simulations using the density of the solid ice with no porosity ($\sim 900 \text{ kg m}^{-3}$). This indicates that the porosity of ring particles is likely to be larger than 50% and the surface layers’ porosity may be even higher. An importance of a network of microcracks was also pointed out by Kouchi et al. (1992), who found very low values of the thermal conductivity of amorphous and crystalline ices (thermal inertia values less than $10 \text{ Jm}^{-2}\text{K}^{-1}\text{s}^{-1/2}$) in their laboratory experiments even though the porosity was low. Overall, the thermal inertia value is a good indication for the structure of regolith layers represented by poorly known quantities such as the porosity. If the particle size is smaller than the thermal skin depth, the interior of the particle is roughly entirely isothermal. In this case, the temperature drop in the shadow increases with decreasing particle size and is rather independent of the thermal inertia. If the particle size is comparable to the thermal skin depth, the temperature drop depends on both thermal inertia and particle size.

Prior to the Cassini mission, the thermal inertia values were estimated using thermal data mostly from ground-based observations. Morrison (1974) and Froidevaux et al. (1981) estimated the thermal inertia of the B ring particles to be $> 40 \text{ Jm}^{-2}\text{K}^{-1}\text{s}^{-1/2}$ and $\sim 13 \text{ Jm}^{-2}\text{K}^{-1}\text{s}^{-1/2}$, respectively, using their ground-based data and applying a simple cooling and heating model

¹The estimated size of regolith particles increases with wavelength. It may indicate the regolith particle size increases with depth in a single ring particle, as longer waves reach to deeper in a ring particle. On the other hand, the estimated size may be biased by observed wavelengths even though regolith particles with different sizes are well mixed regardless of depth.

developed by Aumann and Kieffer (1973). They also found that particles less than about a centimeter should not occupy a significant fraction of the ring cross section. Ferrari et al. (2005) applied their thermal model to their ground based data and estimated the thermal inertias of the B and C rings to be $5_{-2}^{+18} \text{ Jm}^{-2}\text{K}^{-1}\text{s}^{-1/2}$ and $6_{-4}^{+12} \text{ Jm}^{-2}\text{K}^{-1}\text{s}^{-1/2}$, respectively. Leyrat et al. (2008a) analyzed both their ground-based observation data and Voyager IRIS data for the C ring, using their new monolayer model (Ferrari and Leyrat, 2006), and confirmed the very low thermal inertia estimated by Ferrari et al. (2005). The thermal inertia values for the A ring and the Cassini division have not been estimated so far using ring temperatures in Saturn’s shadow.

Since the Saturn orbit insertion of the Cassini spacecraft in July 2004, Cassini CIRS has obtained more than a million spectra ($7 \mu\text{m} - 1\text{mm}$) of Saturn’s rings (Flasar et al., 2005; Spilker et al., 2005, 2006; Altobelli et al., 2007, 2008, 2009; Leyrat et al., 2008b; Flandes et al., 2010). In Paper II, we estimated the albedo and the fraction of fast rotators with a good radial resolution, applying our multilayer model developed in Paper I to the radially scanned CIRS data selected in Spilker et al. (2006). Although the thermal inertia values were also estimated in Paper II, the data sets were not very suitable for accurate measurements of the thermal inertia. For optically thick rings, the thermal inertia was constrained from the temperature difference between the lit and unlit faces, but there was degeneracy between the thermal inertia and the fraction of particles bouncing at the midplane. For optically thin rings, the thermal inertia was constrained from the temperature difference between the morning and evening temperatures, but the accuracy of the estimated thermal inertia was not good because the azimuthal locations of the data points were far from Saturn’s shadow. In the present paper, we analyze azimuthally scanned CIRS data including those in Saturn’s shadow and precisely estimate the thermal inertia values for Saturn’s main rings (the A, B, and C rings and the Cassini division), extensively using our multilayer model. The azimuthally scanned CIRS data have advantages in their spatial and spectral resolutions, azimuthal coverages both inside and outside Saturn’s shadow, and solar phase coverages as compared with previous ground-based and spacecraft (Pioneer and Voyager) observations. Some of azimuthally scanned CIRS data obtained in the early Cassini mission have been already published by Leyrat et al. (2008b). In addition to these data, we use some more data obtained later.

In Sec. 2, we discuss how the thermal relaxation time is related to the thermal inertia and the particle size. In Sec. 3, we explain data selections and fitting procedures and show fitted parameter values. In Sec. 4, we discuss implication from estimated thermal inertia values and future works. A summary is given in Sec. 5.

2. Thermal relaxation time and thermal inertia

The physics of eclipse cooling is summarized as follows. When the illumination on a ring particle changes with a typical frequency ω , its temperature is modified in a surface layer of

characteristic thickness (i.e., thermal skin depth) given as

$$\ell_s = \sqrt{\frac{K}{\rho C \omega}}, \quad (1)$$

where K , ρ , and C are the thermal conductivity, the physical density, and the specific heat of the particle, respectively. For the case of eclipse cooling of Saturn's rings, the time scale of the cycle, $2\pi/\omega$, may be the twice of the eclipse time $2t_{\text{eclip}}$, which is typically ~ 3 hr. The timescale to release the heat in the skin depth when the particle is in Saturn's shadow (i.e., thermal relaxation time for eclipse) is given by

$$t_{\text{rel}} = \frac{4\pi r^2 \ell_s \rho C (T_p - T_{p,0})}{4\pi r^2 \sigma_{\text{SB}} \epsilon (T_p^4 - T_{p,0}^4)} = \frac{\Gamma (T_p - T_{p,0})}{\epsilon \sigma_{\text{SB}} (T_p^4 - T_{p,0}^4) \sqrt{\omega}} \quad (r \gg \ell_s), \quad (2)$$

where r is the radius of the particle, T_p is the particle temperature, $T_{p,0}$ is the particle temperature calculated only using the Saturn's thermal flux, σ_{SB} is the Stefan-Boltzmann constant, ϵ is the thermal emissivity, and $\Gamma = \sqrt{\rho C K}$ is the thermal inertia. The temperature $T_{p,0}$ is expected to be close to the temperature at equinox (when the solar elevation is zero), which occurred in August, 2009 (Spilker et al., 2009; Flandes et al., 2010). If $t_{\text{rel}} \ll t_{\text{eclip}}$, T_p quickly drops to $T_{p,0}$ after particles enter Saturn's shadow. On the other hand, if $t_{\text{rel}} \gg t_{\text{eclip}}$, the temperature drop is negligible. For the typical thermal inertia values of Saturn's ring particles reported in previous works ($\sim 10 \text{ J m}^{-2} \text{ K}^{-1} \text{ s}^{-1/2}$; Ferrari et al., 2005), $t_{\text{rel}} \sim t_{\text{eclip}}$, so the degree of the temperature drop sensitively depends on Γ .

Eq. (2) assumes that the particle size is sufficiently larger than the skin depth ($r \gg \ell_s$). If $r \ll \ell_s$, the thermal relaxation time is given by the larger one of the thermal diffusion time

$$t_{\text{diff}} = \frac{r^2}{K/\rho C} \quad (3)$$

or the time to release the internal energy of whole the hemisphere by radiation

$$t_{\text{rad}} = \frac{\frac{4}{3}\pi r^3 \rho C (T_p - T_{p,0})}{4\pi r^2 \sigma_{\text{SB}} \epsilon (T_p^4 - T_{p,0}^4)} = \frac{1}{3} \frac{\rho C r (T_p - T_{p,0})}{\epsilon \sigma_{\text{SB}} (T_p^4 - T_{p,0}^4)}. \quad (4)$$

The ratio of the two time scale is roughly given as $t_{\text{diff}}/t_{\text{rad}} \sim \sigma_{\text{SB}} T_p^3 r / K$. Substituting typical values for Saturn's rings and considering a particle comparable to the skin depth ($K = 10^{-3} \text{ W m}^{-2} \text{ K}$, $T_p = 90 \text{ K}$, $r = \ell_s \sim 1 \text{ mm}$), one can find that $t_{\text{diff}} \ll t_{\text{rad}}$. This means that the interior of a small particle quickly reaches to isothermal due to heat conduction before the particle cools down by radiation. Thus, the temperature drop of small particles in the shadow depends on the product $\rho C r$ instead of Γ in Eq. (2). When $r \sim \ell_s$, t_{rel} depends on both $\rho C r$ and Γ . In the present paper, we first consider particles sizes sufficiently larger than the skin depth and estimate the thermal inertia values. Then, we make additional fits where size of small particles is varied. Comparison between Eqs. (2) and (4) suggests that decreasing r has an effect similar

to decreasing Γ (i.e., particles tend to react to the input illumination instantaneously in both cases). We will discuss this relation in Sec. 3.3.3 after we estimate Γ and r .

Our thermal model assumes a bimodal spin distribution consisting of slow and fast rotators, while an actual spin distribution of a ring may be continuous. A discussion for the criterion for fast and slow rotators is similar to the above (Farinella et al., 1998). The time scale of the illumination change for a particle spin is the spin period t_{spin} and the corresponding frequency is given by $\omega = 2\pi/t_{\text{spin}}$. The particle is regarded as a fast rotator if $t_{\text{spin}} \ll t_{\text{rel}}$, and as a slow rotator if $t_{\text{spin}} \gg t_{\text{rel}}$. Dynamical simulations for Saturn’s rings (Ohtsuki, 2005; Morishima and Salo, 2006) showed that, for Saturn’s rings, the spin period of the largest particles is comparable to the orbital period t_{orb} and is usually longer than the relaxation time ($t_{\text{spin}} \sim t_{\text{orb}} > t_{\text{rel}}$), while the spin period of small particles is much shorter, as the spin period is roughly proportional to their sizes due to mutual collisions. The fraction of fast rotators f_{fast} (the normal optical depth of fast rotators relative to the total normal optical depth, τ), which is one of the parameters in our model, may be approximately given by the total cross section of particles with $t_{\text{spin}} < t_{\text{rel}}$ relative to the total cross section of all particles. Since t_{rel} depends on Γ , f_{fast} depends on Γ , if a spin (and size) distribution is given. In this paper, we first estimate f_{fast} and Γ as independent parameters, as we did in Papers I and II. Then, we compare estimated values of f_{fast} and Γ with the relation predicted from the above theory using the size distribution estimated in previous observations (French and Nicholson, 2000) (see Sec. 4.3).

3. Parameter fits

3.1. Data selection

The azimuthally scanned CIRS data for the main rings are summarized in Tables 1-4 (observational geometries) and Figs. 1-4 (observed temperatures). Only the scans selected for parameter fits (see below) are shown in these tables and figures, although there are more azimuthal scans. All azimuthally scanned data up to Feb.18 (DOY 49), 2007, including those in our Tables 1, 2, and 4, are shown in Leyrat et al. (2008b). We use some additional data obtained later: the C10 scan for the C ring (Table 1) and all the data for the Cassini division (Table 3). The ring spectra from the CIRS far-infrared channel, named Focal Plane 1 (FP1) are used. As done in all previous works using FP1 spectra (e.g., Spilker et al., 2005, 2006), the ring temperature is obtained by fitting a black body spectrum multiplied by a scale factor to the observed spectrum between 100-400 cm^{-1} (100-25 μm). The scale factor includes the geometric filling factor, the thermal emissivity, and a scalar factor that arises when observing a system comprised of particles at more than one temperatures (Altobelli et al., 2007, Paper II). The spectral resolution for the data ranges from 0.5 to 15.5 cm^{-1} (Flasar et al., 2004).

[Figs. 1-4]
[Tables 1-4]

We select the data for parameter fits taking into account the following points.

1. Data at high solar elevation are favorable (if they exist) since a large temperature drop in Saturn’s shadow allows us to estimate the thermal inertia accurately. For the A ring and

the Cassini division, the eclipse time is too short if solar elevation is large and the data at intermediately high ($\sim 15^\circ$) or lower solar elevations are used.

2. In order to resolve the degeneracy between the albedo and the fraction of fast rotators, it is necessary to make fits to data at low and high solar phases at the same radial location simultaneously. It is desirable that spatial resolutions and solar elevations of these scans are similar.
3. The data for the lit face only are used for the A and B rings. The temperature of the unlit face of an optically thick ring is determined by how efficiently the heat is transported from the lit face to the unlit face and is controlled not only by the thermal inertia but also by the fraction of particles which are hindered from their vertical excursions through the midplane by mutual collisions (Paper II). Therefore, there will be a strong degeneracy between the thermal inertia and the fraction of bouncing particles if we include the unlit face data. We have a more detailed discussion in Sec. 4.2.
4. For the A ring scans, there are azimuthal modulations not only in the absolute thermal brightness but also in the physical temperature due to wakes (Leyrat et al., 2008b; Ferrari et al., 2009). The exact reason why wakes cause temperature modulations is not well known, but this effect is most pronounced when the elevation angle of an observer, $|B|$, is $\sim 10^\circ$ as well as the brightness modulation. Therefore, we need to use data with $|B| \ll 10^\circ$ or $|B| \gg 10^\circ$. For the B ring, the temperature modulation is much smaller even at $|B| \sim 10^\circ$, so we do not remove data by B values.

We find that there are not many data sets available with the above restrictions. The data sets in four radial locations will be used (one location for each ring): 83,000 km, 105,000 km, 120,000 km, and 129,000 km for the C ring, the B ring, the Cassini division, and the A ring, respectively. Since the scans CD1 and CD2 were obtained in the same day and these data have little overlaps in local hour angles, we merge these two scans to a single scan in parameter fits. The azimuthal coverages in the scans CD4, CD5, and CD6 were originally slightly larger than 2π . We removed some of footprints in these scans in order to avoid azimuthal overlaps in a single scan (see Fig. 3). This is just for convenience for our fitting code, and we believe that the impact of removing a small fraction of data on estimated values of parameters is very small.

The optical depth, τ , of each footprint is obtained by averaging a high resolution τ profile over the CIRS FP1 footprint (see Appendix A of Paper II).² The high resolution τ profile from Voyager PPS (Esposito et al., 1983) is used for all rings and another profile from Cassini UVIS (Colwell et al., 2006, 2007) is also used for the A and B rings for comparison. The mean value of τ averaged over all footprints for each scan is shown in Tables 1 to 4 as τ_{PPS} and τ_{UVIS} . These

²In Paper II, the observational geometries used in τ smoothing are those for occultations by PPS and UVIS. Therefore, the smoothed τ is uniquely determined with a given saturnocentric radius, r_p . On the other hand, in this work, the geometries of CIRS observations are used. Thus, the smoothed τ is not always the same even if r_p 's of the footprint centers are the same. The use of CIRS geometries improves fits particularly for the Cassini division.

optical depths are used in simulations. The larger value of τ_{UVIS} than τ_{PPS} is due to wakes. Although our model does not take into account spatial non-uniformity due to wakes, we check how estimated parameters vary with τ for the A and B rings.

3.2. Fitting procedures

We use our multilayer model developed in Paper I and improved in Paper II. Our model solves the equation of classical radiative transfer both in thermal and visible light, taking into account all the heat sources for ring particles including the thermal and reflected visible fluxes from Saturn and the inter-particle heating and scattering. A plane-parallel approximation is adopted, so spatial non-uniformity due to wakes is ignored. Our model adopts a bimodal size distribution consisting of small fast rotators which isotropically emit thermal emissions and large slow rotators represented by non-spinning smooth Lambertian particles. Fast rotators are assumed to have a larger vertical extension than that for slow rotators. Note that the zero-volume filling factor of a ring assumed in classical radiative transfer, a plane-parallel approximation, and smooth spherical particles are probably inappropriate for Saturn’s rings, and fitted parameters may be potentially modified in more advanced models (see also Paper II). The thermal emission from a ring is calculated by integrating thermal emissions from a large number of individual fast and slow rotators. About 3000 particles are used in a single simulation, which is roughly three times larger than those used in Paper II. The most important parameters are the bolometric Bond albedo, A_V , the fraction of fast rotators, f_{fast} , and the thermal inertia, Γ . These three parameters are simultaneously estimated in model fits. Since A_V and f_{fast} were well estimated in Paper II and ring temperatures vary smoothly and monotonically with these two parameters, coarse grids (the grid sizes are typically 0.1 for A_V and 0.2 for f_{fast}) with a few points around the values estimated in Paper II are used for them. On the other hand, fine grids are used for Γ . Ring temperatures in coarse parameter grids are interpolated to those for finer grids for the chi-square fits shown below.

There are some other important input parameters: the size of fast rotators r_{fast} , the optical depth τ , the ratio of the vertical scale height of fast rotators to that of slow rotators h_r , and the type of the vertical motion (whether particles rebound at the midplane or not). As did in Paper II, we vary these parameters and check how sensitively estimated values of A_V , f_{fast} , and Γ are affected. Although there are some uncertainties in these other parameters, the base-line cases, for which the estimated values of parameters are marked boldly in Table 5, give the most reasonable results in Paper II and this work.³ The error size of simulated temperatures is estimated to be less than 0.2 K (while 0.5 K for Paper II). The physical density of 450 kg m^{-3} and the specific heat of $760 \text{ J kg}^{-1} \text{ K}^{-1}$ are used as in Papers I and II. The total time for simulations, by which we estimated parameters shown in Table 5, was about two cpu years. **[Table 5]**

³ In the base-line cases, we assume that $h_r = 3$, except $h_r = 1$ for the B ring, based on dynamical studies (Salo et al., 2001; Morishima and Salo, 2006), and $r_{\text{fast}} = 10 \text{ cm}$. This size of fast rotators is sufficiently larger than the skin depth, ℓ_s . The size of slow rotators is fixed to be 5 m in all cases.

For simulations of a single scan, we use single values of r_p and τ , both averaged over all footprints. This is valid as the dispersions in r_p and τ are usually small enough. Exceptions are scans for the Cassini division, where small changes in radii of footprint centers or spacecraft ranges result in large changes in smoothed τ 's because the τ profiles, obtained in high radial resolution occultations, show large radial variations in this region. Therefore, we take into account the τ variation in different footprints for scans of the Cassini division by conducting two simulations with low and high τ 's and linearly interpolating calculated spectra to the one for a footprint. One clear effect of the τ variation is seen in the CD6 scan (Fig. 3), in which the temperature drops near the noon. This is caused by the mutual shadowing effect, as τ near the noon is largest. Our model succeeds in reproducing this temperature drop (fitting curves are explained in Sec. 3.3).

We make about 100 azimuthal bins and average the elevation B and longitude ϕ_{Cas} of the Cassini spacecraft over the bins. These averaged values are used in simulations. Fine-size bins are used near the shadow lines, as azimuthal temperature variations are large around there. We first calculate thermal spectra in the range of 100-400 cm^{-1} , which is the same range used in deriving observed temperatures, with the spectral resolution of 6 cm^{-1} . Then, these spectra are smoothed over the CIRS FP1 footprints (elongated ellipses on a ring plane) with a gaussian weight.⁴ This smoothing needs to be done not only in the azimuthal direction but also in the radial direction. Since we use a single averaged r_p value for each scan, we assume that ring spectra are uniform in the radial direction and vary only in the azimuthal direction in a footprint. This allows us to avoid conducting different simulations at slightly different radii and save computational time. Applying a black body fit to the smoothed spectrum, we obtain the ring effective (or physical) temperature. In Papers I and II, we did not make smoothing of spectra obtained by simulations because we analyzed thermal data which were azimuthally far from Saturn's shadow and azimuthal temperature variations in footprints were small there.

Using the effective temperatures from observations and simulations, the reduced chi-square χ_0^2 in the three dimensional parameter space $(A_V, f_{\text{fast}}, \Gamma)$ is evaluated. We first calculate the reduced chi-squares for low phase χ_{low}^2 and high phase χ_{high}^2 separately, and take the average of them:

$$\chi_{\text{low}}^2(A_V, f_{\text{fast}}, \Gamma) = \frac{1}{N_{\text{low}} - M} \sum_{n=1}^{N_{\text{low}}} \left(\frac{T_{\text{obs},n} - T_{\text{sim},n}(A_V, f_{\text{fast}}, \Gamma)}{\sigma_{\text{obs},n}} \right)^2 \quad (\text{for } \alpha \leq \alpha_{\text{crit}}), \quad (5)$$

$$\chi_{\text{high}}^2(A_V, f_{\text{fast}}, \Gamma) = \frac{1}{N_{\text{high}} - M} \sum_{n=1}^{N_{\text{high}}} \left(\frac{T_{\text{obs},n} - T_{\text{sim},n}(A_V, f_{\text{fast}}, \Gamma)}{\sigma_{\text{obs},n}} \right)^2 \quad (\text{for } \alpha > \alpha_{\text{crit}}), \quad (6)$$

⁴The full-width half-maximum (FWHM) of CIRS FP1 is 2.51 mrad with a Gaussian fit (Flasar et al. 2004) and the diameter we assume is 5.2 mrad, which covers more than 99% of the signal. The azimuthal extension of the diameter projected on a ring is typically 2-3 degs but exceeds 10 degs for some data with low spatial resolutions. The smoothing procedure is particularly necessary for numerical data whose corresponding observational data have such large azimuthal extensions.

$$\chi_0^2(A_V, f_{\text{fast}}, \Gamma) = \frac{1}{2} \left(\chi_{\text{low}}^2(A_V, f_{\text{fast}}, \Gamma) + \chi_{\text{high}}^2(A_V, f_{\text{fast}}, \Gamma) \right), \quad (7)$$

where N_{low} and N_{high} are the total number of footprints from multiple azimuthal scans at low and high phases, $M(= 3)$ is the number of parameters, n is the index for a footprint, $T_{\text{obs},n}$ and $T_{\text{sim},n}$ are the observed and simulated temperatures for the n -th footprint, $\sigma_{\text{obs},n}$ is the standard error size of the observed temperature (see below), α is the solar phase angle, and α_{crit} is the angle which discriminates low and high phases. We set the error size $\sigma_{\text{obs},n}$ to be larger one of the one obtained from black body fits or the standard deviation of temperatures in azimuthal bins; in most cases, the latter is several times larger than the former (0.2-2.0K). We choose $\alpha_{\text{crit}} = 83.71^\circ$ because a slow rotator illuminated by a single heat source has stronger thermal emission than a fast rotator when $\alpha \leq \alpha_{\text{crit}}$ and vice versa. Values of fitted parameters do not sensitively depend on choice of α_{crit} . The combination of best-fit values of $(A_V, f_{\text{fast}}, \Gamma)$ is derived to minimize χ_0^2 . The error bars are estimated after Press et al. (1986) as follows. The chi-square subtracted by its minimum value at the best-fit parameters is defined as $\Delta\chi_0^2$. The lower and upper limits of a parameter is given by the maximum and minimum values of the parameter on the surface of $\Delta\chi_0^2 = 1$ (68% confidence level of a parameter without regard to other parameters). When the upper or lower limits of parameters are out of coverages in simulations, we extrapolate χ_0^2 to some degree. The B ring data are split into two sets, one at high solar elevations (the scans B1-B4) and another at low elevations (the scans B5-B8), and χ_0^2 's are calculated separately and the average χ_0^2 is taken. The B ring parameters are also estimated for high and low solar elevation cases separately to see whether our model can reproduce the dependence on solar elevation.

We first assume that all particles have the same value of Γ . Later, we consider a case with different values of Γ for slow and fast rotators (Γ_{slow} and Γ_{fast}) and parameter fits will be done similar to the above but in the four dimensional parameter space ($M = 4$). The reduced chi-square for this case is defined as $\chi_1^2(A_V, f_{\text{fast}}, \Gamma_{\text{slow}}, \Gamma_{\text{fast}})$.

In order to see the goodness of the estimated parameters, the reduced chi-square for an individual scan is also calculated as

$$\chi^2(A_V, f_{\text{fast}}, \Gamma) = \frac{1}{N_{\text{foot}} - M} \sum_{n=1}^{N_{\text{foot}}} \left(\frac{T_{\text{obs},n} - T_{\text{sim},n}(A_V, f_{\text{fast}}, \Gamma)}{\sigma_{\text{obs},n}} \right)^2 \quad (\text{for each scan}), \quad (8)$$

where N_{foot} is the number of footprints in each scan shown in Tables 1-4.

3.3. Results

3.3.1. A case with a same thermal inertia for all particles

We first assume that all particles have the same Γ . The coverage of Γ in simulations is 2-79 $\text{Jm}^{-2}\text{K}^{-1}\text{s}^{-1/2}$ with twelve grid points ($\Gamma_i = i(i+1)/2 + 1 \text{ Jm}^{-2}\text{K}^{-1}\text{s}^{-1/2}$ for $i = 1$ to 12). The estimated values of A_V , f_{fast} , and Γ for all cases are listed in Table 5 as $A_{V,0}$, $f_{\text{fast},0}$, and Γ_0 , respectively, and those parameters for the base-line cases are shown in Fig. 5. The best fit **[Fig. 5]**

temperature curves for the base-line cases are given by black solid curves in Figs. 1-4. The values of Γ_0 in units of $\text{Jm}^{-2}\text{K}^{-1}\text{s}^{-1/2}$ for the base-line cases are: 20.0 for the C ring, 13.0 for the B ring, 11.0 for the Cassini division, and 16.2 for the A ring. The values of $A_{\text{V},0}$ and $f_{\text{fast},0}$ are consistent with those estimated in Paper II (see Sec. 4.2 for a more detailed discussion). For the case of the B ring, $A_{\text{V},0}$ estimated with the high $|B'|$ data is lower than that with the low $|B'|$ data. This means that our model underestimates the $|B'|$ dependence of the ring temperature as compared with the observations. Nevertheless, the differences of the estimated parameter values for the high and low $|B'|$ cases remain reasonably small and the parameters estimated using all data simply take intermediate values between those for the high and low $|B'|$ cases. In the followings, we will mainly show the results for the high and low $|B'|$ cases separately, as the reduced chi-square values are much smaller than those for the case using all data.

The contour of the reduced chi-square, $\Delta\chi_0^2$, sliced on the A_{V} vs. Γ plane with $f_{\text{fast}} = f_{\text{fast},0}$ is shown in Fig. 6. If the dispersion of observed temperatures at a given range of azimuthal angle is large, $\Delta\chi_0^2$ becomes flat around the best fit parameters and it makes error sizes larger. The Cassini division is a such case; the large temperature dispersion is probably due to complicated radial structures whose scales are smaller than the CIRS footprint size. The dispersion of observed temperatures is usually small for optically thick rings due to good signal to noise ratio, so that the B ring parameters have small error bars. However, the actual uncertainties of parameters for the B ring are probably larger than at least the difference between the values for the high and low $|B'|$ cases which are larger than the error bars (particularly for A_{V}).

[Fig. 6]

3.3.1.1. Dependence on phase angle

Comparisons of the observed temperatures with the modeled temperatures (black curves) in Figs. 1-4 show that the ring temperatures outside the shadow at both low and high phases are well reproduced by the model with appropriate combinations of $A_{\text{V},0}$ and $f_{\text{fast},0}$ whereas there are systematic deviations between the modeled and observed temperatures in the shadow depending on α . At low α , the shadow temperature is overestimated in the model, or Γ_0 is overestimated (see e.g., the C1 scan). On the other hand, the shadow temperature is underestimated in the model at high phase (e.g., the C3 scan). These facts seem to indicate that Γ increases with α . In order to confirm this trend, we make test fits using fixed A_{V} and f_{fast} for all scans and varying only Γ for different scans. Note that the temperature difference between inside and outside the shadow is controlled almost solely by Γ whereas a change in A_{V} or f_{fast} causes nearly a constant temperature change at all azimuthal locations.

The estimated values of Γ of individual scans for the base-line cases are shown in Fig. 7 and listed in Table 6 as Γ_{ind} . The corresponding temperature curves are given by blue dashed curves in Figs. 1-4. As we expected, Γ_{ind} increases with α for all rings. These trends are verified as the reduced chi-square, χ^2 (shown in Figs. 1-4), for each scan is reduced with α -dependent Γ . In Fig. 7, we also plot the Γ values for the C and B rings estimated by Ferrari et al. (2005). The range of α in their ground based observations is $4.7 - 6.2^\circ$, and their very low Γ values are consistent with our fitting lines for α vs. Γ . For the B ring, if we use A_{V} and f_{fast} estimated using

[Fig. 7]
[Table 6]

all data, the low $|B'|$ case shows lower Γ_{ind} than that for the high $|B'|$ case at similar α (shown only in Table 6 not in Fig. 7), because the temperature outside the shadow is underestimated for the high $|B'|$ case and overestimated for the low $|B'|$ case. On the other hand, the use of different combinations of A_V and f_{fast} gives values of Γ_{ind} consistent each other for both cases.

Although Γ_{ind} depends on α as seen in Fig. 7, it is unlikely that individual particles have α -dependent Γ and their low- Γ faces align toward the Sun because particles are spinning and spin axis orientations change by collisions. A plausible interpretation for the α -dependence of Γ_{ind} is that large slow rotators have lower Γ values than those for small fast rotators. The thermal emission from slow rotators is relatively stronger than that from fast rotators at low phase and vice versa. Therefore, particle groups which are dominant in the thermal emission may vary with phase angle and measured thermal inertias may vary as well. This possibility will be examined in Sec. 3.3.2.

3.3.1.2. Dependence on optical depth and particle bouncing

For the A and B rings, Γ_0 is almost independent of the scale height ratio, h_r , but decreases with increasing optical depth, τ , and takes larger values for the case without bouncing than with bouncing. The latter two dependences indicate that the thermal relaxation time for an optically thick ring depends not only on Γ of individual particles, but also on τ and type of vertical motion, whereas the discussion for the thermal relaxation time in Sec. 2 is for an isolated particle. In order to help understand the latter two dependences, we examine how the ring physical temperature decreases in Saturn's shadow at different vertical locations, $-3 < z/h < 3$, where z is the vertical position and is positive on the lit face and h is the vertical scale height (Fig. 8). Here, the ring physical temperature is given by the averaged temperature over different particles at a certain z (Eq. (27) of Paper I), and all particles are assumed to be fast rotators ($f_{\text{fast}} = 1$) so that the temperature is independent of the direction of emission. For cases with bouncing of particles at the midplane (the top and middle panels of Fig. 8), the energy is transported through the midplane by radiation only, so the unlit face temperature ($z < 0$) is very low and its azimuthal variation is also very small. On the lit face, the ring temperature increases with increasing z when illuminated by the Sun while it decreases with increasing z in Saturn's shadow. These trends are explained by the inter-particle shadowing and heating effects, respectively. The inter-particle heating causes a sort of the green house effect, by which an optically thicker ring can retain the heat relatively longer in the planetary shadow as compared with a thinner ring (compare the top and middle panels of Fig. 8). Since the effective thermal relaxation time of a ring increases with increasing τ for a fixed Γ , an estimated Γ needs to decrease with increasing τ in order to reproduce the observed temperature drop in the shadow. When particles have sinusoidal vertical motion without bouncing, the vertical temperature gradient is small both for the lit and unlit faces (the bottom panel of Fig. 8). In this case, the heat is efficiently removed from both faces, meaning a short thermal relaxation time, as compared with the case with bouncing. Thus, the estimated Γ needs to be relatively larger.

[Fig. 8]

3.3.2. A case with different thermal inertias for slow and fast rotators

In the last section, the thermal inertia value for all particles was assumed to be the same. Here, we make another fit assuming different values of the thermal inertias for slow and fast rotators, Γ_{slow} and Γ_{fast} . This means that the number of the free parameters is now four instead of three. The grids of Γ_{slow} and Γ_{fast} used in simulations are 2, 5, 9, and 15 $\text{Jm}^{-2}\text{K}^{-1}\text{s}^{-1/2}$ and 10, 20, 35, 55, 80, and 120 $\text{Jm}^{-2}\text{K}^{-1}\text{s}^{-1/2}$, respectively. The estimated values of A_V , f_{fast} , Γ_{slow} , and Γ_{fast} are shown in Fig. 5 and listed in Table 5. The corresponding temperature curves are given by red solid curves in Figs. 1-4. The estimated values of A_V and f_{fast} are almost the same with those for the case with a single thermal inertia, Γ_0 . The estimated values of Γ_{slow} and Γ_{fast} for the base-line cases are in the range of 5-9 $\text{Jm}^{-2}\text{K}^{-1}\text{s}^{-1/2}$ and 19-77 $\text{Jm}^{-2}\text{K}^{-1}\text{s}^{-1/2}$, respectively. Although the values of Γ_{fast} are large, they are still much lower than that for solid ice with no porosity ($\sim 2600 \text{Jm}^{-2}\text{K}^{-1}\text{s}^{-1/2}$). Therefore, fast rotators are likely to have surface regolith layers, but they may be not as fluffy as those for slow rotators. The most likely reason for larger Γ_{fast} than Γ_{slow} is that the centrifugal force for fast rotators is so strong that fluffy regolith particles cannot stay on fast rotators.

Unfortunately, the error bars for Γ_{slow} and Γ_{fast} are larger than those for Γ_0 , because of the increased freedom in adjusting temperature drops in the planetary shadow: although slow rotators are dominant emitters at low phase, the contribution from fast rotators is not unimportant and similarly the slow rotators' contribution is not unimportant at high phase. Figure 9 shows contours of $\Delta\chi_1^2$ on the Γ_{slow} vs. Γ_{fast} plane with the best-fit values of A_V and f_{fast} . One can find that $\Delta\chi_1^2$ is very flat along the Γ_{fast} axis and the error bars for Γ_{fast} are not well determined for some cases. This happens particularly if f_{fast} is small (B ring, low $|B'|$) or the scatter in the observed temperature is large (the Cassini division). However, it is obvious that $\Gamma_{\text{fast}} > \Gamma_{\text{slow}}$ for all rings. [Fig. 9]

Parameter fits are clearly improved by using different values of Γ_{slow} and Γ_{fast} , as the lowest χ_1^2 (with the best-fit parameters) is lower than the lowest χ_0^2 for all rings. Indeed, the chi-square for an individual scan, χ^2 , is also reduced for almost all scans for all rings. Although the α -dependent systematic deviations between the modeled and observed temperatures in the shadow are much reduced, they are not completely removed, as χ^2 is still larger than that for the α -dependent Γ case. This is probably because our model assumes a bimodal size distribution whereas an actual ring has a continuous size distribution. The distribution of the thermal inertia is likely to be continuous as well. Therefore, Γ for the largest particles may be even smaller than Γ_{slow} , which is the thermal inertia averaged over a certain size range of large particles. Similarly, Γ for the smallest particles may be larger than Γ_{fast} . This effect needs to be investigated in future works.

3.3.3. Lower limit of the size of fast rotators

As discussed in Sec. 2, fitting results shown in Secs. 3.3.1 and 3.3.2 are not altered even if we use different particle sizes as long as the particle size is sufficiently larger than the thermal

skin depth. If we use particle sizes as small as or even smaller than the skin depth, reducing particle size causes an effect similar to reducing thermal inertia. Eqs. (2) and (4) suggest the following relation:

$$r \simeq \frac{3\Gamma}{\rho C \sqrt{\omega}}. \quad (9)$$

Since the use of a too small r makes fits worse, the lower limit of the size of particles can be constrained. Here we make additional parameter fits varying size of fast rotators, r_{fast} . The number of parameters to be fitted is now five instead of four in Sec. 3.3.2. We define the lower limit size of fast rotators, $r_{\text{fast,min}}$, as the lowest r_{fast} giving $\Delta\chi_1^2 = 1$ in the five dimensional parameter space.⁵ This is similar to the definitions of the lower limits of other parameters estimated in previous sections. Since a comprehensive coverage of the five dimensional parameter space is computationally so intense that the following effective method to estimate $r_{\text{fast,min}}$ is adopted. We first fix all four parameters (A_V , f_{fast} , Γ_{slow} , and Γ_{fast}) estimated in Sec. 3.3.2 and search for a size of fast rotators, r_2 , which gives $\Delta\chi_1^2 \sim 1$. Then, we make parameter fits varying four other parameters at $r_{\text{fast}} = r_2$ and $0.5r_2$. When other parameters vary, $\Delta\chi_1^2$ is usually smaller than 1 for $r_{\text{fast}} = r_2$. This means that $r_{\text{fast,min}}$ should be at least smaller than r_2 . Linearly interpolating $\Delta\chi_1^2$ for $r_{\text{fast}} = r_2$ and $0.5r_2$, we estimate $r_{\text{fast,min}}$, where $\Delta\chi_1^2 = 1$.

The values of χ_1^2 for $r_{\text{fast}} \sim r_2$ and other estimated parameters are listed in Table 5. We find that $r_{\text{fast,min}}$ ranges from 1-10 mm. The temperature curves for $r_{\text{fast}} \sim r_{\text{fast,min}}$ are shown as purple dotted curves in Figs. 1-4. Figure 10 compares $r_{\text{fast,min}}$ with the lower limit of Γ_{fast} , $\Gamma_{\text{fast,min}}$, for the base-line cases ($r_{\text{fast}} = 10$ cm) (note if $\Gamma_{\text{fast}} = 33.5^{+71.6}_{-15.5} \text{ Jm}^{-2}\text{K}^{-1}\text{s}^{-1/2}$, $\Gamma_{\text{fast,min}}$ is $18.0 \text{ Jm}^{-2}\text{K}^{-1}\text{s}^{-1/2}$). For the B ring at low $|B'|$ and the Cassini division, we were not able to estimate $\Gamma_{\text{fast,min}}$. For other three rings, for which the values of $\Gamma_{\text{fast,min}}$ are well estimated, the relations between $r_{\text{fast,min}}$ and $\Gamma_{\text{fast,min}}$ are well represented by Eq. (9) with $r = r_{\text{fast,min}}$ and $\Gamma = \Gamma_{\text{fast,min}}$. There, the cycle of the illumination change, $2\pi/\omega$, needs to be specified to determine the thermal skin depth. We find that a cycle which gives a reasonable fit is somewhere between the twice of the eclipse time $2t_{\text{eclip}}$ (see Tables 1-4 for t_{eclip}) and the orbital period t_{orb} .⁶ We think that this is reasonable, because temperatures of ring particles recover almost immediately after they exit Saturn's shadow, but not completely, and their temperatures gradually increase until they enter Saturn's shadow again.

[Fig. 10]

⁵Correction factors $(N_{\text{low}} - 4)/(N_{\text{low}} - 5)$ and $(N_{\text{high}} - 4)/(N_{\text{high}} - 5)$ are ignored, as N_{low} and N_{high} are sufficiently large.

⁶The orbital periods are 6.78 hr for the C ring (83,000 km), 9.65 hr for the B ring (105,000 km), 11.79 hr for the Cassini division (120,000 km), and 13.14 hr for the A ring (129,000 km).

4. Discussion

4.1. Interpretations

The estimation of $r_{\text{fast},\text{min}}$ in Sec. 3.3.3 means that particles with sizes equal to or less than $r_{\text{fast},\text{min}}$ should not occupy more than f_{fast} of the total cross section. This condition seems to be satisfied for all rings, as the lower cutoff r_{min} for the continuous size distribution estimated in French and Nicholson (2000) (Table 7) is comparable to or larger than $r_{\text{fast},\text{min}}$. Therefore, the quantity constrained by the eclipse cooling is the thermal inertia, not the size of ring particles. [Table. 7]

In Sec. 3.3.2, we found $\Gamma_{\text{fast}} > \Gamma_{\text{slow}}$ for all the rings. The most likely reason for this is that small fast rotators cannot hold very fluffy regolith layers because of their fast spins. Dynamical studies (Salo, 1987; Ohtsuki, 2005; Morishima and Salo, 2006) show that the spin period is about the orbital period for the largest particles and is roughly proportional to the particle size for an extended size distribution. The centrifugal force is comparable to the self-gravity on a particle with a synchronous rotation near the Roche limit, around which Saturn’s main rings exist. Therefore, the centrifugal force well exceeds the self-gravity on surfaces of small particles. Since Γ_{fast} is likely to be still much smaller than the thermal inertia of the solid ice with no porosity, some regolith particles probably stick to small fast rotators due to the surface energy (Choksi et al., 1993, Albers et al., 2006). The regolith layers of fast rotators may also be compacted by mutual impacts whose velocities are larger than the velocity dispersion of large particles (Salo, 1992; Morishima and Salo, 2006). Alternatively, small particles might be regolith free. In this case, as suggested by Kouchi et al. (1992), microcracks would be responsible for Γ_{fast} . In any case, it is expected that the thermal inertia increases with decreasing size of a ring particle. A similar size dependence of the thermal inertia is also found in asteroids (Delbo and Tanga, 2009). However, the mechanism causing the size dependence is probably different from that for Saturn’s ring particles; their interpretation is that large asteroids (> 100 km) are primordial and collisional debris build up thick regolith layers on them whereas small bodies are fragments in catastrophic impacts between large bodies.

In the interpretation of the variations of Γ_{slow} and Γ_{fast} in different rings, we need to consider (1) the distribution of $\Gamma(r)$ as a function of particle size r and (2) the ratio of the smallest particle size r_{min} to the largest particle size r_{max} for actual rings with continuous size distribution. As we discussed in Sec. 3.3.2, the thermal inertia of the largest particles, $\Gamma(r = r_{\text{max}})$, may be close to Γ_{slow} or slightly less. Therefore, $\Gamma(r = r_{\text{max}})$ seems to be similar for all the rings, except the Cassini division has a lower $\Gamma(r = r_{\text{max}})$. Because Γ is likely to increase with decreasing r , as discussed above, Γ_{fast} is expected to increase with decreasing $r_{\text{min}}/r_{\text{max}}$. On the other hand, Γ_{fast} for the A ring is larger than that for the C and B rings, even though $r_{\text{min}}/r_{\text{max}}$ (A ring) = $r_{\text{min}}/r_{\text{max}}$ (B ring) $>$ $r_{\text{min}}/r_{\text{max}}$ (C ring) (Table 7). This means that with a same r/r_{max} (< 1), an A ring particle has the largest Γ . Thus, the size dependence of Γ for the A ring is steeper than those for the B and C rings, whereas Γ_{fast} for the C ring larger than that for the B ring may be explained by the smaller $r_{\text{min}}/r_{\text{max}}$ for the C ring. The large Γ_{fast} for the A ring is probably due to wakes (Salo, 1995; Colwell et al., 2006; Hedman et al., 2007). Dynamical simulations (Morishima and Salo, 2006) including the self-gravity show that the spin frequency increases with increasing r_p

for a fixed dynamical optical depth. The self-gravity also steepens size dependence of the spin frequency. The collision velocity between large particles are usually slow as they are in the same wake, while small particles floating in inter-wake spaces suffer collisions with impact velocities as fast as the velocity dispersion of wakes, which is much larger than the escape velocity of individual particles. Therefore, for small particles with a certain r/r_{\max} ($\ll 1$), both the spin frequency and the collision velocity are largest in the A ring. These facts may explain large Γ_{fast} for the A ring, while Γ_{slow} for the A ring is similar to those for the C and B rings. It should be noted again that the spatial non-uniformity due to wakes is not directly taken into account in our model. The discussion here was based on the estimated values of Γ_{fast} for the standard cases and readers are cautioned that the uncertainty in Γ_{fast} is very large.

The Cassini division has the smallest Γ_{slow} among the Saturn’s main rings. This smallest value seems to be real, as Γ_{ind} in Fig. 7 at a given α always shows the smallest value, except at very large α (i.e., the CD3 scan). The very small value of Γ_{slow} may indicate that there are some dust sources around this region and ring particles are fluffily coated by these grains. There are at least two dusty ringlets in the Cassini division (Horányi et al., 2009): one in the Huygens gap (117,490 km) and another in the Laplace gap (119,940 km) called the Charming ringlet (Hedman et al., 2010). In particular, the location of the latter one is very close to the centers of the CIRS footprints of azimuthal scans. These dusty ringlets themselves are very tenuous and unimportant for the direct thermal emission. However, their existence indicates injection of small grains into this region by some unknown mechanisms, as they are likely to be very young (less than a few thousand years old; Hedman et al., 2010). The small lower-cutoff size for the Cassini division found in French and Nicholson (2000) (Table 7) also seems consistent with a relatively large population of dust. They also inferred that there is a substantial variation in the particle size distribution across this region, with relatively more small particles in the inner than in the outer Cassini division (reported also in Colwell et al. (2009)). This probably indicates that the dust sources are limited to the inner Cassini division. The value of Γ_{ind} for the CD3 scan which looks remarkably too large as compared with those for other scans seems to be explained by the fact that the saturnocentric distance of the CD3 scan is slightly larger than those for other scans (by ~ 2000 km at shadow lines). Howett et al. (2010) found that the thermal inertias of saturnian satellites from Rhea inward have relatively lower values ($\sim 10 \text{ Jm}^{-2}\text{K}^{-1}\text{s}^{-1/2}$) than those for Iapetus and Phoebe ($\sim 20 \text{ Jm}^{-2}\text{K}^{-1}\text{s}^{-1/2}$), which are located farther away from Saturn. They indicated that this is probably related to coating by E-ring material ejected from Enceladus’ plumes. Similar things may happen also in Saturn’s rings although dust sources are different.

The large value of χ_0^2 for the B ring in the case using all data comes from the fact that our model underestimates $|B'|$ dependence of the ring temperature, as we stated in Sec. 3.3.1. By separately estimating parameters for the B ring at the high and low $|B'|$ cases, the values of χ_0^2 are remarkably reduced. However, χ_0^2 for the high $|B'|$ case is still much larger than unity. The phase angles for the scans B2, B3, and B4 are low. In Fig. 2, with decreasing phase angle from $\sim 40^\circ$ (the B4 scan) to $\sim 10^\circ$ (the B2 scan), the observed temperature outside the shadow increases by $\sim 4\text{K}$, whereas the modeled temperature increases by only $\sim 1\text{K}$. Therefore, our model underestimates not only $|B'|$ dependence but also α dependence at low phase. The steep α

dependence observed is probably due to the thermal opposition surge caused by packing of ring particles into thin layers (Altobelli et al., 2009). The effect of particle packing is also known to enhance $|B'|$ dependence of photometric brightness for dense rings (Salo and Karjalainen, 2003), but it is uncertain if it is also the case for the thermal emission. For more accurate estimations of particle properties for optically thick rings such as the B and A rings, this packing effect and the effect due to wakes need to be taken into account in future models. Nevertheless, we believe that parameters estimated in the present work are not so different from actual values, because the deviations between observed and modeled temperatures remain reasonably small.

4.2. Toward estimations of radial variation of thermal inertia

We have estimated the thermal inertia values for only four radial points in this study (one point for each ring), and it is desirable to examine the radial variation of the thermal inertia in each ring. Unfortunately, azimuthal scans were taken at only a limited number of radial points by Cassini CIRS and it is probably difficult to cover a sufficiently large number of radial points even in the extended mission. However, there are some quasi-radial scans along the shadow lines and in Saturn’s shadow. Even if we use reasonable sets of shadow scans, precise estimation of Γ is not simple in the optically thick rings (the A and B rings) because an estimated Γ depends on types of vertical motion of ring particles and adopted τ (Table 5).

The degeneracy between Γ and the type of vertical motion can be resolved if we combine Γ estimated from the temperature difference between the lit and unlit faces (Paper II) and Γ estimated from the eclipse cooling (this work). Figure 11 shows comparisons of parameters estimated in Paper II (solid lines) and this work (diamonds) for the case with τ_{PPS} . Here we use Γ_0 from this study because Paper II did not consider different values of Γ for slow and fast rotators. For the B and A rings, estimated parameters for the bouncing model are shown with black lines. Very good agreements between both studies are found if we assume the bouncing model for the B ring and the non-bouncing model for the other rings. In fact, with the non-bouncing model, Γ and A_V for the A ring from this study are slightly higher and lower than those from Paper II. These deviations are fixed if we assume a small fraction of particles rebound at the midplane, because both Γ from Paper II and A_V from this study increase with increasing fraction of bouncing particles.

[Fig. 11]

There is still a problem in fitted parameters due to their dependences on τ . The uncertainty in τ for the A and B rings comes from wakes (Colwell et al., 2006, 2007), so ultimately more sophisticated models, which take into account wakes, are necessary. However, the uncertainty in estimated values of Γ due to the uncertainty of τ seems very small, as we will see below. Figure 12 shows Γ for the mid B ring (105,000 km) estimated from this study (the mean values of Γ_0 for high B' and low B' cases) and from Paper II (Γ_{PII}) as a function of the fraction of bouncing particles f_b for two different cases of optical depths, τ_{PPS} and τ_{UVIS} . Here, $f_b = 0$ and 1 represent the non-bouncing and bouncing models, respectively, and a linear dependence of Γ on f_b is assumed between $f_b = 0$ and 1. In this work, we did not estimate Γ_0 for the case

[Fig. 12]

with $f_b = 0$ and τ_{UVIS} , and we assume that the ratio $\Gamma_0(\tau_{\text{PPS}})/\Gamma_0(\tau_{\text{UVIS}})$ is independent of f_b as well as the ratio of the error sizes. The values of Γ and f_b on the crossing points of the solid and dashed lines are the predicted values. For the case with τ_{PPS} , the crossing point has $\Gamma \simeq 10\text{--}13 \text{ Jm}^{-2}\text{K}^{-1}\text{s}^{-1/2}$ and $f_b \simeq 1$. On the other hand, for the case with τ_{UVIS} , the crossing point has $\Gamma = 14 \text{ Jm}^{-2}\text{K}^{-1}\text{s}^{-1/2}$ and $f_b = 0.27$. Since we used the possible minimum value, $40 \text{ Jm}^{-2}\text{K}^{-1}\text{s}^{-1/2}$, for $\Gamma_{\text{PH}}(\tau_{\text{UVIS}})$ at $f_b = 1$, Γ and f_b at the cross point will be respectively higher and lower than those shown in Fig. 12. Nevertheless, Γ at the crossing point should not be larger than $\Gamma_0(\tau_{\text{UVIS}})$ at $f_b = 0$ ($\sim 15 \text{ Jm}^{-2}\text{K}^{-1}\text{s}^{-1/2}$). Therefore, even though we cannot resolve the degeneracy between τ and f_b , similar values of Γ seem to be obtained regardless of the choice of τ . This discussion needs to be extended to the case with different values of Γ_{slow} and Γ_{fast} in future works.

4.3. Criteria of slow and fast rotators

We have treated the thermal inertia Γ and the fraction of fast rotators f_{fast} as independent parameters in data fitting. However, they are not independent of each other if the spin (and size) distribution is given. Here, we discuss the relation between Γ and f_{fast} . A similar discussion is found in Sec. 5.2 of Paper I.

We adopt the size distribution estimated in French and Nicholson (2000) (Table 7). The number density per unit size $n(r)$ is given by a power-law as $n(r) \propto r^{-q}$ ($r_{\text{min}} \leq r \leq r_{\text{max}}$), where r_{min} and r_{max} are the minimum and maximum size of particles, respectively. They estimated the size distribution using diffracted stellar light, and their results are consistent with those from radio occultation (Zebker et al., 1985; Cuzzi et al., 2009). From dynamical studies (Ohtsuki, 2005, 2006; Morishima and Salo, 2006), the particle spin period is approximately given as

$$t_{\text{spin}}(r) = C_1 \frac{r}{r_{\text{max}}} t_{\text{orb}}, \quad (10)$$

where C_1 is the numerical constant and depends on r_p and τ ; we take $C_1 = 2.0, 1.0, 2.0,$ and 0.5 for the C ring, the B ring, the Cassini division, and the A ring from Fig. 11 of Morishima and Salo (2006). The critical particle size, which discriminates slow and fast rotators, is defined as

$$t_{\text{spin}}(r_{\text{crit}}) = t_{\text{rel}}, \quad (11)$$

where t_{rel} is the thermal relaxation time given by Eq. (2) with $\omega = 2\pi/t_{\text{spin}}$. The critical size r_{crit} is given as

$$\frac{r_{\text{crit}}}{r_{\text{max}}} = \frac{1}{2\pi C_1 t_{\text{orb}}} \left(\frac{\Gamma(T_p - T_{p,0})}{\epsilon \sigma_{\text{SB}}(T_p^4 - T_{p,0}^4)} \right)^2. \quad (12)$$

Here, Γ is the thermal inertia for particles with $r = r_{\text{crit}}$, which should be somewhere between Γ_{slow} and Γ_{fast} . In a comparison below, we assume that $\Gamma = \Gamma_0$ as a nominal value. The temperature, $T_{p,0}$ is supposed to be derived from the flux to the night-side hemisphere of a particle, and we take its value from the equinox data assuming the night-side hemisphere is illuminated

only by Saturn: 65 K for the C ring and 48 K for other rings (Spilker et al., 2009). If we simply regard a particle with $r < r_{\text{crit}}$ as a fast rotator and a particle with $r \geq r_{\text{crit}}$ as a slow rotator, the fraction of fast rotators in cross section f_{fast} is given as

$$f_{\text{fast}} = \frac{(r_{\text{crit}}/r_{\text{max}})^{3-q} - (r_{\text{min}}/r_{\text{max}})^{3-q}}{1 - (r_{\text{min}}/r_{\text{max}})^{3-q}}. \quad (13)$$

Eqs.(12) and (13) indicate that f_{fast} increases with increasing Γ and decreasing T_p and t_{orb} , for given $r_{\text{min}}/r_{\text{max}}$ and q .

Figure 13 shows the relation between Γ and f_{fast} derived from Eqs. (10) - (13) with $r_{\text{min}}/r_{\text{max}}$ and q from French and Nicholson (2000). The estimated values, Γ_0 and $f_{\text{fast},0}$, from our parameter fits (Table 5) are also plotted. We find good agreements between values from our parameter fits and the theoretical prediction for all rings. In Paper II, we discussed that our model probably underestimates f_{fast} due to the lack of the effects of packing of ring particles and surface roughness. The good agreements seen in Fig. 13 may indicate that these effects do not largely change estimated values of parameters such as f_{fast} and Γ . For the A and B rings, we may need to use a larger $T_{p,0}$ due to the mutual heating. In this case, f_{fast} predicted from Eq. (13) will be lower than those shown in Fig. 13 and the agreements will be even better unless $T_{p,0}$ is very close to T_p .

[Fig. 13]

5. Conclusions

In the present paper, we have estimated the thermal inertia values of Saturn’s main rings by applying our thermal model to azimuthally scanned spectra taken by the Cassini CIRS instrument. Model fits show the thermal inertia of ring particles to be: 16_{-5}^{+10} , 13_{-4}^{+4} , 20_{-6}^{+10} , and 11_{-6}^{+68} $\text{Jm}^{-2}\text{K}^{-1}\text{s}^{-1/2}$ for the A, B, and C rings and the Cassini division, respectively. However, there are systematic deviations between modeled and observed temperatures in Saturn’s shadow depending on solar phase angle. Test fits, which allow individual scans taken at different solar phase angles to have different thermal inertia values, show that the apparent thermal inertia increases with solar phase angle. This dependence is likely to be explained, if large slowly spinning particles have lower thermal inertia values than those for small fast spinning particles, because the thermal emission of the slow rotators is relatively stronger than that of fast rotators at low phase and vice versa. We made additional parameter fits, which assume that slow and fast rotators have different thermal inertia values. The estimated thermal inertia values of slow rotators are 8_{-4}^{+19} , 8_{-3}^{+10} , 9_{-9}^{+23} , and 5_{-5}^{+37} $\text{Jm}^{-2}\text{K}^{-1}\text{s}^{-1/2}$ for the A, B, and C rings and the Cassini division, respectively, and those of fast rotators are 77_{-66}^{+123} , 27_{-27}^{+173} , 34_{-16}^{+71} , 55_{-55}^{+145} $\text{Jm}^{-2}\text{K}^{-1}\text{s}^{-1/2}$. The values for fast rotators are still much smaller than those for the solid ice with no porosity. Thus, fast rotators are likely to have surface regolith layers, but these may be not as fluffy as those for slow rotators, probably because the capability of holding regolith particles is limited for fast rotators due to the centrifugal force. The large thermal inertia of fast rotators for the A ring is probably due to wakes, which largely enhance spin and collision velocities of small particles. The low thermal inertia of the Cassini division probably indicates that there are some

dust sources around this region and ring particles are fluffily coated by dust. Other additional parameter fits, in which size of fast rotators is varied, indicate that particles less than ~ 1 cm should not occupy more than a half of the cross section for the A, B, and C rings. This is consistent with previous estimations of the ring particle size distribution.

Acknowledgments

We thank Cedric Leyrat and an anonymous reviewer for their comments, which improved our manuscript. We are grateful for the support by the Cassini project and the NASA's OPR and PGG Programs. K.O. is also grateful for the support by JSPS KAKENHI (22340125). We thank Nicholas Altobelli and Stu Piorz for developing the CIRS database, Scott Edgington, Shawn Brooks and Mark Showalter for designing the CIRS ring observations. R.M. thanks the UVIS ring team in LASP for fruitful discussions. Numerical simulations were carried out with the supercomputers, Nebula and Galaxy, at JPL.

REFERENCES

- Albers, N., Spahn, F., 2006. The influence of particle adhesion on the stability of agglomerates in Saturn's rings. *Icarus* 181, 292–301.
- Altobelli, N., Spilker, L.J., Piorz, S., Brooks, S., Edgington, S., Wallis, B., Flasar, M., 2007. C ring fine structures revealed in the thermal infrared. *Icarus* 191, 691–701.
- Altobelli, N., Spilker, L.J., Leyrat, C., Piorz, S., 2008. Thermal observations of Saturn's main rings by Cassini CIRS: Phase, emission and solar elevation dependence. *Planet. Space Sci.* 56, 134–146.
- Altobelli, N., Spilker, L.J., Piorz, S., Leyrat, C., Edgington, S., Wallis, B., Flandes, A., 2009. Thermal phase curves observed in Saturn's main rings by Cassini-CIRS: Detection of an opposition effect? *Geophys. Res. Lett.* 36, L10105.
- Aumann, H.H., Kieffer, H.H., 1973. Determination of particle sizes in Saturn's rings from their eclipse cooling and heating curves. *Astrophys. J.* 186, 305–311.
- Bradley, E.T. Colwell, J.E., Esposito, L.W., Cuzzi, J.N., Tollerud, H., Chambers, L., 2010. Far ultraviolet spectral properties of Saturn's rings from Cassini UVIS. *Icarus* 206, 458–466.
- Choksi, A., Tielens, A.G.G.M., Hollenbach, D., 1993 Dust coagulation. *Astrophys. J.* 407, 806–819.
- Colwell, J.E., Esposito, L.W., Sremčević, M., 2006. Self-gravity wakes in Saturn's A ring measured by stellar occultations from Cassini. *Geophys. Res. Lett.* 33, L07201.

- Colwell, J.E., Esposito, L.W., Sremčević, M., Stewart, G.R., McClintock, W.E., 2007. Self-gravity wakes and radial structure of Saturn's B ring. *Icarus*, 190, 127–144.
- Colwell, J.E., Cooney, J.H., Esposito, L.W., Sremčević, M., 2009. Density waves in Cassini UVIS stellar occultations: 1. The Cassini Division. *Icarus* 200, 574–580.
- Cuzzi, J.N., Clark, K., Filacchione, G., French, R., Jhonson, R., Marouf, E., Spilker, L., 2009. Ring particle composition and size distribution. In: Dougherty, M.K., Esposito, L.W., Krimigis, S.M. (Eds.), *Saturn from Cassini-Huygens*. Springer, Berlin, pp. 459–509.
- D'Aversa, E., Bellucci, G., Nicholson, P.D., Hedman, M.M., Brown, R.H., Showalter, M.R., Altieri, F., Carrozzo, F.G., Filacchione, G., Tosi, F., 2010. The spectrum of a Saturn ring spoke from Cassini/VIMS. *Geophys. Res. L.* 37, L01203.
- Delbo, M., Tanga, P., 2009. Thermal inertia of main belt asteroids smaller than 100 km from IRAS data. *Planetary and Space Sci.* 57, 259-265.
- Dones, L., Cuzzi, J.N., Showalter, M.R., 1993. Voyager photometry of Saturn's A ring. *Icarus* 105, 184–215.
- Esposito, L.W., O'Callaghan, M., Simmons, K.E., Hord, C.W., West, R.A., Lane, A.L., Pomphrey, R.B., Coffeen, D.L., Sato, M., 1983. Voyager photopolarimeter stellar occultation of Saturn's rings. *J. Geophys. Res.* 88, 8643–8649.
- Farinella, P., Vokorouhlický, D., Hartmann, W.K., 1998. Meteorite delivery via Yarkovsky orbital drift. *Icarus* 132, 378–387.
- Ferrari, C., Leyrat, C., 2006. Thermal emission of spherical spinning ring particles: The standard model. *Astron. Astrophys.* 447, 745–760.
- Ferrari, C., Galdemard, P., Lagage, P.O., Pantin, E., Quoirin, C., 2005. Imaging Saturn's rings with CAMIRAS: thermal inertia of B and C rings. *Astron. Astrophys.* 441, 379–389.
- Ferrari, C., Brooks, S., Edgington, S., Leyrat, C., Pilorz, S., Spilker, L., 2009. Structure of self-gravity wakes in Saturn's A ring as measured by Cassini CIRS. *Icarus* 199, 145–153.
- Flandes, A., Spilker, L.J., Morishima, R., Pilorz, S., Leyrat, C., Altobelli, N., Brooks, S.M., Edgington, S.G., 2010. Brightness of Saturn's rings with decreasing solar elevation. *Planet and Space Science* 58, 1758–1765.
- Flasar, F.M., and 44 colleagues, 2004. Exploring the Saturn system in the thermal infrared: The composite infrared spectrometer. *Space Science Rev.* 115, 169–297.
- Flasar, F.M., and 45 colleagues, 2005. Temperatures, winds, and composition in the Saturnian system. *Science* 307, 1247–1251.
- French, R.G., Nicholson, P.D., 2000. Saturn's rings II. Particle sizes inferred from stellar occultation data. *Icarus* 145, 502–523.

- Froidevaux, L., 1981. Saturn's rings: Infrared brightness variation with solar elevation. *Icarus* 46, 4–17.
- Froidevaux, L., Matthews, K., Neugebauer, G., 1981. Thermal response of Saturn's ring particles during and after eclipse. *Icarus* 46, 18–26.
- Hedman, M.M., Nicholson, P.D., Salo, H., Wallis, B.D. Buratti, B.J., Baines, K.H., Brown, R.H., Clark, R.N., 2007. Self-gravity wake structures in Saturn's A ring revealed by Cassini VIMS. *Astron. J.* 133, 2624–2629.
- Hedman, M.M., Burt, J.A., Burns, J.A., Tiscareno, M.S., 2010. The shape and dynamics of a heliotropic dusty ringlet in the Cassini division. *Icarus* 210, 284–297.
- Horányi, M., Burns, J.A., Hedman, M.M., Jones, G.H., Kempf, S., 2009. Diffuse rings. In: Dougherty, M.K., Esposito, L.W., Krimigis, S.M. (Eds.), *Saturn from Cassini-Huygens*. Springer, Berlin, pp. 511–536.
- Howett, C.J.A., Spencer, J.R., Peral, J., Segura, M., 2010. Thermal inertia and bolometric Bond albedo values for Mimas, Enceladus, Tethys, Dione, Rhea, and Iapetus as derived from Cassini/CIRS measurements. *Icarus* 206, 573–593.
- Kouchi, A., Greenberg, J.M., Yamamoto, T., Mukai, T., 1992. Extremely low thermal conductivity of amorphous ice: relevance to comet evolution. *Astrophys. J.* 388, L73–L76.
- Leyrat, C., Ferrari, C., Charnoz, S., Deciem, J., Spilker, L., Pilorz, S., 2008a. Spinning particles in Saturn's C ring from mid-infrared observations: Pre-Cassini results. *Icarus* 196, 625–641.
- Leyrat, C., Spilker, L., Altobelli, N., Pilorz, S., Ferrari, C., 2008b. Infrared observations of Saturn's rings by Cassini CIRS : Phase angle and local time dependence *Planet. Space Sci.* 56, 117–133.
- Marouf, E.A., Tyler, G.L., Zebker, H.A., Simpson, R.A., Eshleman, V.R., 1983. Particle size distributions in Saturn's rings from Voyager 1 radio occultation. *Icarus* 54, 189–211.
- Morishima, R., Salo, H., 2006. Simulations of dense planetary rings IV: Rotating self-gravitating particles with size distribution. *Icarus* 181, 272–291.
- Morishima, R., Salo, H., Ohtsuki, K., 2009 (Paper I). A multilayer model for thermal infrared emission of Saturn's rings: Basic formulation and implications for Earth-based observations. *Icarus* 201, 634–654.
- Morishima, R., Spilker, L., Salo, H., Ohtsuki, K., Altobelli, N., Pilorz, S., 2010 (Paper II). A multilayer model for thermal infrared emission of Saturn's rings. II: Albedo, spins, and vertical mixing of ring particles inferred from Cassini CIRS. *Icarus* 210, 330–345.
- Morrison, D., 1974. Infrared radiometry of the rings of Saturn. *Icarus* 22, 57–65.

- Nicholson, P.D., and 15 coauthors, 2008. A close look at Saturn's rings with Cassini VIMS. *Icarus* 193, 182-212.
- Ohtsuki, K., 2005. Rotation rates of particles in Saturn's rings. *Astrophys. J.* 626, L61–L64.
- Ohtsuki, K., 2006. Rotation rate and velocity dispersion of planetary ring particles with size distribution II. Numerical simulation for gravitating particles. *Icarus* 183, 384–395.
- Poulet, F., Cruikshank, D.P., Cuzzi, J.N., Roush, T.L., French, R.G., 2003. Composition of Saturn's rings A, B, and C from high resolution near-infrared spectroscopic observations. *Astron. Astrophys.* 412, 305–316.
- Press, W.H., Teukolsky, S.A., Vetterling, W.T., Flannery, B.P., 1986. *Numerical Recipes*. Cambridge Univ. Press, Cambridge, UK.
- Salo, H., 1987. Numerical simulations of collisions between rotating particles. *Icarus* 70, 37–51.
- Salo, H., 1992. Numerical simulations of dense collisional systems. II - Extended distribution of particle sizes. *Icarus* 96, 85–106.
- Salo, H., 1995. Simulations of dense planetary rings. III. Self-gravitating identical particles. *Icarus* 117, 287–312.
- Salo, H., Karjalainen, R., 2003. Photometric modeling of Saturn's rings I. Monte Carlo method and the effect of nonzero volume filling factor. *Icarus* 164, 428–460.
- Salo, H., Schmidt, J., Spahn, F., 2001. Viscous overstability in Saturn's B ring I. Direct simulations and measurement of transport coefficients. *Icarus* 153, 295–315.
- Shoshany, Y., Prialnik, D., Podolak, M., 2002. Monte Carlo modeling of the thermal conductivity of porous cometary ice. *Icarus* 157, 219–227.
- Spilker, L.J., Pilorz, S.H., Edgington, S.G., Wallis, B.D., Brooks, S.M., Pearl, J.C., Flasar, F.M., 2005. Cassini CIRS observations of a roll-off in Saturn ring spectra at submillimeter wavelengths. *Earth, Moon, and Planets* 96, 149–163.
- Spilker, L.J., and 11 colleagues, 2006. Cassini thermal observations of Saturn's main rings: Implications for particle rotation and vertical mixing. *Planet. Space Sci.* 54, 1167–1176.
- Spilker, L.J., Flandes, A., Morishima, R., Altobelli, N., Leyrat, C., Pilorz, S., Ferrari, C.C., Edgington, S.G., Brooks, S.M., 2009. Saturn ring temperatures at equinox with Cassini CIRS. American Geophysical Union, Fall Meeting 2009, abstract #P51B-1131.
- Stuart, S.J., Stewart, G.R., Lewis, M.C., Colwell, J.E., Sremčević, M., 2010. Estimating the masses of Saturn's A and B rings from high-optical depth *N*-body simulations and stellar occultations. *Icarus* 206, 431–445.

Zebker, H.A., Marouf, E.A., Tyler, G.L., 1985. Saturn's rings - Particle size distributions for thin layer model. *Icarus* 64, 531–548.

| Scan No. | Date | N_{foot} | a_{\odot} (AU) | B' (deg) | B (deg) | α (deg) | ϕ_p (deg) | r_p (1,000 km) | ϕ_{Cas} (deg) | r_{Cas} (r_{Sat}) | τ_{PPS} | t_{eclip} (hr) |
|----------|--------|-------------------|---------------------|---------------|--------------|-------------------|-------------------|---------------------|------------------------------|--|---------------------|----------------------------|
| C1 | 05-156 | 1610 | 9.076 | -21.48 | -18.73 | 41.38 | 261.10 (co) | 83.10 | 143.00 | 26.30 | 0.108 | 1.56 |
| | | | | | -20.02 | 34.67 | 17.25 | 82.81 | 135.78 | 24.46 | | |
| C2 | 05-176 | 1979 | 9.079 | -21.28 | -20.20 | 30.51 | 276.91 (co) | 83.11 | 157.85 | 19.19 | 0.111 | 1.56 |
| | | | | | -22.30 | 20.64 | 27.82 | 82.80 | 147.23 | 17.08 | | |
| C3 | 05-178 | 1711 | 9.079 | -21.25 | 9.59 | 125.27 | 286.54 (cl) | 83.59 | 59.99 | 11.18 | 0.107 | 1.57 |
| | | | | | 9.55 | 121.33 | 1.69 | 82.39 | 55.75 | 10.56 | | |
| C4 | 05-194 | 1764 | 9.081 | -21.09 | -19.88 | 28.25 | 22.05 (cl) | 83.08 | 151.57 | 21.31 | 0.110 | 1.57 |
| | | | | | -21.76 | 26.49 | 100.21 | 82.81 | 149.83 | 19.03 | | |
| C5 | 06-300 | 1126 | 9.164 | -15.29 | -22.66 | 112.84 | 283.54 (cl) | 83.76 | 60.10 | 12.92 | 0.111 | 1.66 |
| | | | | | -28.19 | 107.66 | 1.37 | 82.90 | 56.61 | 10.88 | | |
| C6 | 06-337 | 2482 | 9.172 | -14.77 | 60.00 | 113.76 | 270.33 (cl) | 83.58 | 289.52 | 12.77 | 0.111 | 1.67 |
| | | | | | 50.03 | 105.73 | 89.70 | 82.91 | 276.30 | 9.98 | | |
| C7 | 07-016 | 1041 | 9.181 | -14.16 | -48.86 | 45.17 | 297.13 (cl) | 83.11 | 171.86 | 13.40 | 0.112 | 1.67 |
| | | | | | -53.71 | 37.09 | 119.60 | 82.42 | 146.87 | 11.96 | | |
| C8 | 07-048 | 1132 | 9.188 | -13.70 | -25.66 | 117.50 | 281.25 (cl) | 84.54 | 51.69 | 18.54 | 0.114 | 1.68 |
| | | | | | -29.92 | 114.26 | 2.20 | 82.66 | 49.87 | 16.82 | | |
| C9 | 07-049 | 2188 | 9.189 | -13.69 | -52.95 | 80.11 | 92.11 (co) | 83.92 | 100.70 | 16.47 | 0.114 | 1.68 |
| | | | | | -59.23 | 72.70 | 301.52 | 82.93 | 86.40 | 15.09 | | |
| C10 | 07-082 | 982 | 9.196 | -13.22 | -50.18 | 75.22 | 346.88 (cl) | 84.01 | 101.22 | 9.97 | 0.113 | 1.69 |
| | | | | | -60.14 | 72.80 | 74.78 | 81.49 | 97.32 | 9.10 | | |

Table 1: Geometry data of azimuthal scans for the C ring. Date is year and day of year, N_{foot} is the number of footprints (or spectra), a_{\odot} is the heliocentric distance, B' is the solar elevation angle, B is the elevation angle of the Cassini spacecraft, α is the solar phase angle, ϕ_p is the local hour angle (or the longitude) of ring particles around Saturn with the origin at the midnight, r_p is the saturnocentric distance, ϕ_{Cas} is the longitude of the spacecraft around the footprint, r_{Cas} is the range of the spacecraft (r_{Sat} is the radius of Saturn), τ_{PPS} is the mean optical depth from observations taken by Voyager PPS (see the text), and t_{eclip} is the mean time of the eclipse. For B , α , r_p , ϕ_{Cas} , and r_{Cas} , the upper and lower limits of each parameter are shown in the upper and lower rows. For ϕ_p , the values of initial and last foot prints during the scans are shown in the upper and lower rows. The characters in the parenthesis in the upper row of ϕ_p represents the azimuthal direction of the scan: “co” is for a counter-clockwise scan whereas “cl” for a clockwise scan.

| Scan No. | Date | N_{foot} | a_{\odot} (AU) | B' (deg) | B (deg) | α (deg) | ϕ_p (deg) | r_p (1,000 km) | ϕ_{Cas} (deg) | r_{Cas} (r_{Sat}) | τ_{PPS} | τ_{UVIS} | t_{eclip} (hr) |
|----------|--------|-------------------|---------------------|---------------|--------------|-------------------|-------------------|---------------------|------------------------------|--|---------------------|----------------------|----------------------------|
| B1 | 04-184 | 503 | 9.042 | -24.46 | -14.89 | 105.93 | 284.21 (cl) | 107.08 | 66.12 | 26.06 | 1.660 | 2.491 | 1.24 |
| | | | | | -16.65 | 103.95 | 26.65 | 105.60 | 64.34 | 24.00 | | | |
| B2 | 05-158 | 1533 | 9.076 | -21.46 | -19.81 | 13.01 | 18.90 (cl) | 106.12 | 171.23 | 15.79 | 1.856 | 3.204 | 1.42 |
| | | | | | -24.53 | 8.19 | 139.28 | 105.21 | 166.20 | 12.25 | | | |
| B3 | 05-175 | 1372 | 9.078 | -21.29 | -18.72 | 34.25 | 0.40 (cl) | 105.01 | 145.79 | 25.29 | 1.572 | 2.279 | 1.44 |
| | | | | | -21.15 | 31.98 | 108.99 | 104.76 | 143.57 | 22.20 | | | |
| B4 | 05-229 | 1353 | 9.086 | -20.70 | -18.60 | 43.78 | 357.03 (cl) | 105.37 | 141.26 | 26.67 | 1.570 | 2.277 | 1.47 |
| | | | | | -20.80 | 36.28 | 277.87 | 104.46 | 133.19 | 23.81 | | | |
| B5 | 06-300 | 1571 | 9.164 | -15.29 | -26.29 | 107.06 | 17.21 (co) | 106.29 | 65.12 | 12.08 | 1.877 | 3.228 | 1.67 |
| | | | | | -30.13 | 103.58 | 269.10 | 104.92 | 60.30 | 10.29 | | | |
| B6 | 07-016 | 1311 | 9.181 | -14.16 | -39.76 | 43.16 | 152.84 (co) | 105.53 | 180.02 | 13.85 | 1.877 | 3.460 | 1.70 |
| | | | | | -56.28 | 26.73 | 287.33 | 104.27 | 166.05 | 11.50 | | | |
| B7 | 07-048 | 1515 | 9.188 | -13.70 | -29.06 | 114.20 | 28.36 (co) | 106.02 | 55.24 | 18.40 | 1.857 | 3.135 | 1.71 |
| | | | | | -31.53 | 111.16 | 283.54 | 104.78 | 49.87 | 16.20 | | | |
| B8 | 07-049 | 822 | 9.189 | -13.69 | -51.02 | 86.44 | 356.27 (cl) | 106.84 | 85.26 | 15.97 | 1.974 | 4.014 | 1.72 |
| | | | | | -56.91 | 82.08 | 82.35 | 104.97 | 75.37 | 14.99 | | | |

Table 2: Same as Table 1 but for the B ring. Here the mean optical depth from observations taken by Cassini UVIS, τ_{UVIS} , is also shown, in addition to τ_{PPS} .

| Scan No. | Date | N_{foot} | a_{\odot} (AU) | B' (deg) | B (deg) | α (deg) | ϕ_p (deg) | r_p (1,000 km) | ϕ_{Cas} (deg) | r_{Cas} (r_{Sat}) | τ_{PPS} | t_{eclip} (hr) |
|----------|--------|-------------------|---------------------|---------------|--------------|-------------------|-------------------|---------------------|------------------------------|--|---------------------|----------------------------|
| CD1 | 07-098 | 402 | 9.200 | -12.99 | -49.76 | 83.85 | 28.68 (cl) | 120.84 | 94.65 | 6.82 | 0.069 | 1.76 |
| | | | | | -56.03 | 77.02 | 60.91 | 119.69 | 81.68 | 6.36 | | |
| CD2 | 07-098 | 1126 | 9.200 | -12.99 | -41.76 | 70.27 | 30.93 (co) | 120.95 | 124.91 | 9.19 | 0.097 | 1.76 |
| | | | | | -53.53 | 59.19 | 300.20 | 118.61 | 104.98 | 7.24 | | |
| CD3 | 07-130 | 2678 | 9.207 | -12.53 | 41.60 | 150.90 | 314.45 (cl) | 121.84 | 337.04 | 8.06 | 0.149 | 1.77 |
| | | | | | 23.76 | 140.37 | 98.20 | 119.81 | 324.19 | 6.76 | | |
| CD4 | 08-015 | 2364 | 9.270 | -8.82 | 57.92 | 117.62 | 359.99 (co) | 120.04 | 300.32 | 8.67 | 0.095 | 1.88 |
| | | | | | 34.87 | 84.08 | 0.03 | 119.76 | 252.06 | 6.49 | | |
| CD5 | 08-027 | 2767 | 9.273 | -8.64 | 57.37 | 109.88 | 359.97(co) | 120.18 | 289.68 | 9.55 | 0.100 | 1.88 |
| | | | | | 36.83 | 79.59 | 0.02 | 119.74 | 245.31 | 7.48 | | |
| CD6 | 08-262 | 3328 | 9.337 | -5.04 | -31.83 | 53.11 | 293.87 (cl) | 121.79 | 158.53 | 13.75 | 0.121 | 1.94 |
| | | | | | -45.36 | 39.20 | 289.98 | 118.92 | 135.06 | 10.36 | | |

Table 3: Same as Table 1 but for the Cassini division.

| Scan No. | Date | N_{foot} | a_{\odot} (AU) | B' (deg) | B (deg) | α (deg) | ϕ_p (deg) | r_p (1,000 km) | ϕ_{Cas} (deg) | r_{Cas} (r_{Sat}) | τ_{PPS} | τ_{UVIS} | t_{eclip} (hr) |
|----------|--------|-------------------|---------------------|---------------|--------------|-------------------|-------------------|---------------------|------------------------------|--|---------------------|----------------------|----------------------------|
| A1 | 06-300 | 2626 | 9.164 | -15.28 | -25.60 | 106.56 | 269.34 (cl) | 129.79 | 74.88 | 12.39 | 0.432 | 0.598 | 1.64 |
| | | | | | -45.43 | 92.41 | 90.64 | 128.80 | 55.34 | 7.83 | | | |
| A2 | 07-016 | 1061 | 9.181 | -14.15 | -35.16 | 28.72 | 311.93 (cl) | 129.58 | 194.27 | 14.31 | 0.445 | 0.618 | 1.71 |
| | | | | | -40.40 | 21.09 | 134.59 | 128.06 | 168.26 | 11.75 | | | |
| A3 | 07-048 | 2619 | 9.188 | -13.70 | -24.38 | 118.18 | 260.41 (cl) | 130.72 | 59.09 | 19.44 | 0.441 | 0.596 | 1.73 |
| | | | | | -38.54 | 106.19 | 87.43 | 128.55 | 47.15 | 15.47 | | | |

Table 4: Same as Table 2 but for the A ring.

| Ring | τ | h_r | Bouncing | r_{fast} | Γ_{slow} | Γ_{fast} | AV | f_{fast} | χ_1^2 | Γ_0 | AV_0 | $f_{\text{fast},0}$ | χ_0^2 |
|---------------------|----------------------|-------|----------|-------------------|---|--|---|---|--------------|--|---|---|--------------|
| C ring | τ_{PPS} | 3 | no | 10 cm | 8.5^{+22.8}_{-8.5} | 33.5^{+71.6}_{-15.6} | 0.14^{+0.06}_{-0.09} | 0.68^{+0.11}_{-0.10} | 1.58 | 20.0^{+10.1}_{-5.7} | 0.12^{+0.06}_{-0.12} | 0.68^{+0.10}_{-0.10} | 2.25 |
| | | | | 1 cm | 15.1 ^{+29.9} _{-11.9} | 80.0 ^{+120.0} _{-65.9} | 0.17 ^{+0.22} _{-0.11} | 0.58 ^{+0.42} _{-0.15} | 2.51 | | | | |
| | | | | 5 mm | 20.0 ^{+80.0} _{-7.0} | 80.0 ^{+120.0} _{-70.4} | 0.14 ^{+0.10} _{-0.14} | 0.58 ^{+0.42} _{-0.13} | 5.82 | | | | |
| B ring (all) | τ_{PPS} | 1 | yes | 10 cm | 5.0^{+4.7}_{-3.1} | 45.0^{+145.0}_{-25.1} | 0.58^{+0.01}_{-0.01} | 0.49^{+0.14}_{-0.13} | 18.62 | 13.0^{+2.1}_{-2.1} | 0.58^{+0.01}_{-0.01} | 0.35^{+0.13}_{-0.10} | 19.66 |
| | τ_{PPS} | 1 | yes | 10 cm | 7.4^{+4.9}_{-2.9} | 35.0^{+92.7}_{-16.5} | 0.56^{+0.01}_{-0.01} | 0.48^{+0.12}_{-0.08} | 7.91 | 14.3^{+1.8}_{-2.5} | 0.56^{+0.01}_{-0.01} | 0.42^{+0.11}_{-0.07} | 9.38 |
| B ring (high B') | | | | 1 cm | 8.0 ^{+6.1} _{-2.8} | 80.0 ^{+120.0} _{-80.0} | 0.56 ^{+0.02} _{-0.01} | 0.42 ^{+0.08} _{-0.17} | 8.36 | | | | |
| | | | | 5 mm | 14.0 ^{+6.6} _{-3.3} | 80.0 ^{+120.0} _{-70.8} | 0.56 ^{+0.02} _{-0.01} | 0.34 ^{+0.09} _{-0.15} | 10.33 | | | | |
| B ring (low B') | τ_{PPS} | 3 | yes | 10 cm | 6.1 ^{+5.3} _{-1.4} | 150.0 ^{+50.0} _{-130.1} | 0.57 ^{+0.01} _{-0.01} | 0.20 ^{+0.04} _{-0.05} | 8.27 | 13.9 ^{+1.6} _{-1.8} | 0.56 ^{+0.01} _{-0.01} | 0.17 ^{+0.04} _{-0.04} | 9.72 |
| | τ_{UVIS} | 1 | yes | 10 cm | 8.4 ^{+4.5} _{-3.8} | 20.0 ^{+46.5} _{-7.1} | 0.60 ^{+0.01} _{-0.01} | 0.42 ^{+0.13} _{-0.12} | 5.96 | 12.3 ^{+1.9} _{-1.5} | 0.60 ^{+0.01} _{-0.01} | 0.37 ^{+0.09} _{-0.09} | 6.65 |
| Cassini div. | τ_{PPS} | 1 | no | 10 cm | 5.0 ^{+8.1} _{-1.2} | 39.5 ^{+56.0} _{-6.6} | 0.29 ^{+0.01} _{-0.02} | 0.75 ^{+0.04} _{-0.12} | 10.13 | 21.3 ^{+5.3} _{-2.8} | 0.31 ^{+0.01} _{-0.01} | 0.58 ^{+0.08} _{-0.08} | 12.16 |
| | τ_{PPS} | 1 | yes | 10 cm | 9.1^{+8.9}_{-4.4} | 19.0^{+181.0}_{-19.0} | 0.64^{+0.02}_{-0.01} | 0.27^{+0.22}_{-0.27} | 1.72 | 11.7^{+3.6}_{-2.5} | 0.64^{+0.01}_{-0.02} | 0.23^{+0.20}_{-0.21} | 1.80 |
| Cassini div. | | | | 1 mm | 18.4 ^{+22.7} _{-6.3} | 35.0 ^{+165.0} _{-35.0} | 0.62 ^{+0.02} _{-0.03} | 0.21 ^{+0.26} _{-0.25} | 2.51 | | | | |
| | | | | 0.5 mm | 19.0 ^{+81.0} _{-6.2} | 55.0 ^{+145.0} _{-55.0} | 0.62 ^{+0.03} _{-0.02} | 0.18 ^{+0.24} _{-0.18} | 2.85 | | | | |
| Cassini div. | τ_{PPS} | 3 | yes | 10 cm | 10.1 ^{+5.7} _{-4.5} | 20.0 ^{+180.0} _{-20.0} | 0.65 ^{+0.02} _{-0.01} | 0.06 ^{+0.11} _{-0.06} | 1.66 | 11.7 ^{+3.5} _{-2.5} | 0.65 ^{+0.01} _{-0.02} | 0.05 ^{+0.10} _{-0.05} | 1.79 |
| | τ_{UVIS} | 1 | yes | 10 cm | 8.4 ^{+3.8} _{-3.6} | 8.5 ^{+191.5} _{-8.5} | 0.71 ^{+0.02} _{-0.02} | 0.02 ^{+0.33} _{-0.02} | 2.39 | 8.7 ^{+1.8} _{-1.9} | 0.70 ^{+0.02} _{-0.02} | 0.03 ^{+0.28} _{-0.03} | 2.16 |
| Cassini div. | τ_{PPS} | 1 | no | 10 cm | 15.9 ^{+84.1} _{-10.5} | 11.5 ^{+40.3} _{-11.5} | 0.50 ^{+0.29} _{-0.04} | 0.38 ^{+0.29} _{-0.20} | 2.22 | 14.6 ^{+5.0} _{-3.6} | 0.49 ^{+0.02} _{-0.03} | 0.42 ^{+0.19} _{-0.19} | 2.38 |
| | τ_{PPS} | 3 | no | 10 cm | 4.7 ^{+36.4} _{-4.7} | 55.0 ^{+145.0} _{-35.0} | 0.43 ^{+0.08} _{-0.09} | 0.46 ^{+0.26} _{-0.22} | 1.26 | 11.0 ^{+67.7} _{-6.2} | 0.42 ^{+0.08} _{-0.08} | 0.50 ^{+0.24} _{-0.25} | 1.46 |
| A ring | | | | 2 mm | 15.0 ^{+85.0} _{-13.8} | 5.0 ^{+195.0} _{-5.0} | 0.41 ^{+0.12} _{-0.17} | 0.53 ^{+0.47} _{-0.50} | 2.10 | | | | |
| | | | | 1 mm | 15.0 ^{+85.0} _{-11.2} | 5.0 ^{+195.0} _{-5.0} | 0.41 ^{+0.12} _{-0.17} | 0.45 ^{+0.55} _{-0.45} | 3.02 | | | | |
| A ring | τ_{PPS} | 3 | no | 10 cm | 7.8^{+18.9}_{-4.2} | 76.5^{+123.5}_{-65.8} | 0.49^{+0.03}_{-0.03} | 0.62^{+0.12}_{-0.11} | 1.54 | 16.2^{+10.3}_{-5.1} | 0.49^{+0.03}_{-0.03} | 0.62^{+0.11}_{-0.11} | 1.93 |
| | | | | 1 cm | 10.0 ^{+49.9} _{-7.5} | 35.0 ^{+165.0} _{-30.0} | 0.49 ^{+0.04} _{-0.04} | 0.61 ^{+0.16} _{-0.19} | 1.98 | | | | |
| A ring | | | | 5 mm | 20.0 ^{+80.0} _{-15.8} | 10.0 ^{+190.0} _{-10.0} | 0.50 ^{+0.03} _{-0.04} | 0.58 ^{+0.17} _{-0.16} | 2.99 | | | | |
| | τ_{PPS} | 1 | no | 10 cm | 9.0 ^{+19.4} _{-5.7} | 35.0 ^{+165.0} _{-23.6} | 0.49 ^{+0.03} _{-0.03} | 0.69 ^{+0.09} _{-0.11} | 1.52 | 16.2 ^{+10.3} _{-4.7} | 0.49 ^{+0.03} _{-0.03} | 0.68 ^{+0.10} _{-0.12} | 1.86 |
| A ring | τ_{UVIS} | 3 | no | 10 cm | 9.4 ^{+15.5} _{-5.1} | 42.5 ^{+157.5} _{-34.7} | 0.46 ^{+0.03} _{-0.03} | 0.52 ^{+0.22} _{-0.14} | 1.68 | 15.3 ^{+10.8} _{-4.6} | 0.46 ^{+0.03} _{-0.03} | 0.52 ^{+0.12} _{-0.15} | 2.02 |

Table 5: Input and estimated parameters. The base-line case for each ring is shown with bold numbers. The unit for Γ_{slow} , Γ_{fast} , and Γ_0 is $\text{Jm}^{-2}\text{K}^{-1}\text{s}^{-1/2}$. The upper limits of Γ_{slow} and Γ_{fast} are set to be 100 and $200 \text{ Jm}^{-2}\text{K}^{-1}\text{s}^{-1/2}$, respectively, due to insufficient coverages in simulations. The reduced chi-squares, χ_1^2 and χ_0^2 , represent the minimum values in the parameter spaces.

| No. | α (degs) | Γ_{ind} ($\text{Jm}^{-2}\text{K}^{-1}\text{s}^{-1/2}$) | No. | α (degs) | Γ_{ind} ($\text{Jm}^{-2}\text{K}^{-1}\text{s}^{-1/2}$) |
|-------------|--------------------|---|-----|--------------------|---|
| C2 | 25.56 | $13.6^{+6.5}_{-4.2}$ | B2 | 9.63 | $6.8^{+2.1}_{-0.9}$ ($6.3^{+1.9}_{-0.8}$) |
| C4 | 26.95 | $11.9^{+3.6}_{-2.5}$ | B6 | 31.59 | $10.0^{+2.3}_{-1.6}$ ($7.0^{+1.5}_{-0.8}$) |
| C1 | 37.68 | $15.7^{+5.9}_{-3.9}$ | B3 | 32.62 | $10.8^{+1.6}_{-1.1}$ ($11.5^{+1.9}_{-1.3}$) |
| C7 | 39.23 | $15.4^{+9.4}_{-5.0}$ | B4 | 40.05 | $12.2^{+2.1}_{-1.7}$ ($11.9^{+2.1}_{-1.5}$) |
| C10 | 73.56 | $17.8^{+11.5}_{-6.1}$ | B8 | 83.37 | $12.9^{+2.6}_{-2.3}$ ($7.1^{+1.3}_{-0.5}$) |
| C9 | 74.62 | $16.6^{+12.9}_{-6.0}$ | B1 | 104.17 | $16.5^{+2.6}_{-1.7}$ ($21.1^{+3.7}_{-2.7}$) |
| C6 | 106.23 | $24.5^{+56.3}_{-12.2}$ | B5 | 104.71 | $15.7^{+7.9}_{-3.9}$ ($9.2^{+1.8}_{-1.8}$) |
| C5 | 109.61 | $27.3^{+50.1}_{-11.5}$ | B7 | 111.93 | $11.5^{+3.4}_{-2.0}$ ($6.9^{+1.5}_{-0.7}$) |
| C8 | 115.37 | $21.6^{+26.2}_{-8.0}$ | | | |
| C3 | 122.47 | $29.2^{+10.6}_{-5.6}$ | | | |
| CD6 | 46.26 | $5.1^{+13.8}_{-3.3}$ | A2 | 24.08 | $13.9^{+5.7}_{-3.5}$ |
| CD1 and CD2 | 70.61 | $9.7^{+17.4}_{-4.9}$ | A1 | 96.95 | $26.4^{+73.6}_{-12.2}$ |
| CD5 | 96.39 | $10.2^{+89.8}_{-7.2}$ | A3 | 108.52 | $26.1^{+58.0}_{-11.2}$ |
| CD4 | 102.67 | $10.5^{+89.5}_{-7.2}$ | | | |
| CD3 | 142.19 | $20.2^{+65.2}_{-10.4}$ | | | |

Table 6: Thermal inertia of an individual scan, Γ_{ind} , for the base-line cases, derived with fixed $A_{V,0}$ and $f_{\text{fast},0}$. The scans are on the order of the mean value of the phase angle, α . The upper limit of Γ_{ind} is set to be $100 \text{ Jm}^{-2}\text{K}^{-1}\text{s}^{-1/2}$ due to an insufficient coverage in simulations. The different combinations of $A_{V,0}$ and $f_{\text{fast},0}$ for the high $|B'|$ case (B1-B4) and the low $|B'|$ case (B5-B8) are used. For comparison, the values of Γ_{ind} estimated using a single combination of $A_{V,0}$ and $f_{\text{fast},0}$ for all the B ring data are shown in parenthesis.

| Ring | r_{min} (cm) | r_{max} (m) | q |
|------------------|--------------------------|-------------------------|------|
| C ring | 1 | 10 | 3.1 |
| B ring | 30 | 20 | 2.75 |
| Cassini division | 0.1 | 20 | 2.75 |
| A ring (inner) | 30 | 20 | 2.75 |

Table 7: The lower and upper cut-off sizes and the power-law index of ring particles estimated in French and Nicholson (2000). The inner A ring is the inside the Encke division.

Figure captions

- Fig. 1. Azimuthal temperature variations for the C ring. The title of each panel is the scan number, which is on the order of the scan date, whereas the panels are placed on the order of the phase angle, α . Green crosses are observed temperatures. Curves are modeled temperatures with best-fit parameters for four different cases: (1) a single value of the thermal inertia (Γ_0) is used for all particles in all scans (black solid curves), (2) different scans can have different values of the thermal inertia Γ_{ind} while A_V and f_{fast} are fixed for all scans (blue dashed curves), (3) the thermal inertias for slow and fast rotators have different values, Γ_{slow} and Γ_{fast} , whose values are shared in all scans (red solid curves), and (4) the same as (3) except the size of fast rotators, r_{fast} , is 5 mm (purple dotted curves). See Table 5 for other fitted parameters. The values of Γ , Γ_{slow} , and Γ_{fast} shown in panels are in units of $\text{Jm}^{-2}\text{K}^{-1}\text{s}^{-1/2}$. The values for the reduced chi-square, χ^2 , for each scan are also shown in parentheses. The mean solar phase angle, α , is shown on the top left of each panel.
- Fig. 2. Same as Fig. 1 but for the B ring. The panels are placed on the order of the phase angle but separately for the high B' scans (B1-B4) and the low B' scans (B5-B8). The purple dotted curve is the case of $r_{\text{fast}} = 5$ mm for the high B' scans and $r_{\text{fast}} = 1$ mm for the low B' scans.
- Fig. 3. Azimuthal variations of the temperature (top) and the optical depth averaged over a footprint (bottom) for the Cassini division. The purple dotted curve is the case of $r_{\text{fast}} = 1$ mm.
- Fig. 4. Same as Fig. 1, but for the A ring. The purple dotted curve is the case of $r_{\text{fast}} = 5$ mm.
- Fig. 5. Bolometric Bond albedo, fraction of fast rotators, and thermal inertia for the Saturn's main rings for the base-line cases. The same thermal inertia value for all particles is assumed in the derivation of $A_{V,0}$, $f_{\text{fast},0}$, and Γ_0 (black crosses), whereas different thermal inertias for slow and fast rotators are assumed in the derivation of A_V (red diamonds), f_{fast} (red diamonds), Γ_{slow} (blue diamonds), and Γ_{fast} (red triangles). See also Table 5.
- Fig. 6. Contour of the reduced chi-square, $\Delta\chi_0^2$, sliced on the A_V vs. Γ plane with the best-fit value of the fraction of fast rotators, $f_{\text{fast},0}$ (from Table 5). Note that the error bars are estimated using the surface of $\Delta\chi_0^2 = 1.0$ in the three dimensional parameter space and displaying these sliced contours is only for the purpose of giving some insights on error bars at other confidence levels (the surfaces of $\Delta\chi_0^2 = 1.00, 2.71, \text{ and } 6.63$ give confidence levels of 68.3 %, 90%, and 99%).
- Fig. 7. Thermal inertia Γ_{ind} vs. phase angle α for the base-line cases. In the parameter fits, $A_V (= A_{V,0})$ and $f_{\text{fast}} (= f_{\text{fast},0})$ are fixed for all scans in each ring, but the thermal inertia is treated as a free parameter. The solid lines represent linear fits of Γ_{ind} from all scans. The values of Γ_{ind} for the C and B rings at $\alpha = 4.7 - 6.2^\circ$ are from Ferrari et al. (2005) (the offset in α between these two data is for avoiding overlaps of the marks but ground-based

observations for both rings were done simultaneously in two different campaigns). The values of Γ_{ind} are also shown in Table 6.

Fig. 8. Contour of ring physical temperature on the plane of the vertical and azimuthal locations. The vertical coordinate z normalized by the scale height h is positive on the lit face. Three cases with different combinations of τ and type of vertical motion are shown. The used parameters are as follows: the heliocentric distance is 9.1 AU, $B' = 21^\circ$, $r_p = 105,000$ km, $A_V = 0.6$, $f_{\text{fast}} = 1.0$, and $\Gamma = 13 \text{ Jm}^{-2}\text{K}^{-1}\text{s}^{-1/2}$. The vertical dashed lines represent shadow lines.

Fig. 9. Contour of the normalized reduced chi-square, $\Delta\chi_1^2$, sliced on the Γ_{slow} vs. Γ_{fast} plane with the best-fit values of A_V and f_{fast} (from Table 5). Note that the error bars are estimated in the four dimensional parameter space and displaying these sliced contours is only for the purpose of giving some insights on error bars at various confidence levels.

Fig. 10. Lower limit of size of fast rotators $r_{\text{fast,min}}$ vs. lower limit of thermal inertia of fast rotators $\Gamma_{\text{fast,min}}$. The size r_{fast} is fixed to be 10 cm for the estimation of $\Gamma_{\text{fast,min}}$. The lines represent theoretical predictions (Eq. (9)) for three different illumination cycles, $2\pi/\omega$. The values of $\Gamma_{\text{fast,min}}$ for the B ring at low B' and the Cassini division are not well estimated and assumed to be $1 \text{ Jm}^{-2}\text{K}^{-1}\text{s}^{-1/2}$.

Fig. 11. Comparison of fitted parameters between this work and Paper II. The solid curves are from Paper II (dotted curves are error sizes) and diamonds are from this work. The scale height ratio h_r is assumed to be 3 except $h_r = 1$ for the B ring. The thermal inertia of all particles is assumed to be the same. The red lines and marks are for the case with standard sinusoidal vertical motion without bouncing whereas the black lines and marks are for the case with cycloidal motion which assumes particle bouncing at the midplane. The values for the B ring from this work are the mean values of high B' and low B' . The radial offset between the red and black diamonds for the B ring is for avoiding overlaps of the marks.

Fig. 12. Thermal inertia as a function of fraction of bouncing particles f_b for the mid B ring. The solid lines are the thermal inertia estimated from this study, Γ_0 , and the dashed lines are the thermal inertia estimated in Paper II, Γ_{PII} . Two cases of optical depth profiles, τ_{PPS} and τ_{UVIS} , are considered in both works. The value of Γ_{PII} for the case with τ_{UVIS} and $f_b = 1$ is uncertain due to the limited coverage in parameter fits in Paper II, but at least larger than $40 \text{ Jm}^{-2}\text{K}^{-1}\text{s}^{-1/2}$. The offsets in f_b are for avoiding overlaps of the marks: the simulations were made for either $f_b = 0$ or 1.

Fig. 13. Thermal inertia vs. fraction of fast rotators for the Saturn's main rings. Black bars represent the range of these parameters directly estimated in model fits to observed data (Γ_0 and $f_{\text{fast},0}$). The red and blue curves are relations between these two parameters predicted from Eqs. (10) - (13) with the size distribution from French and Nicholson (2000) (Table 7).

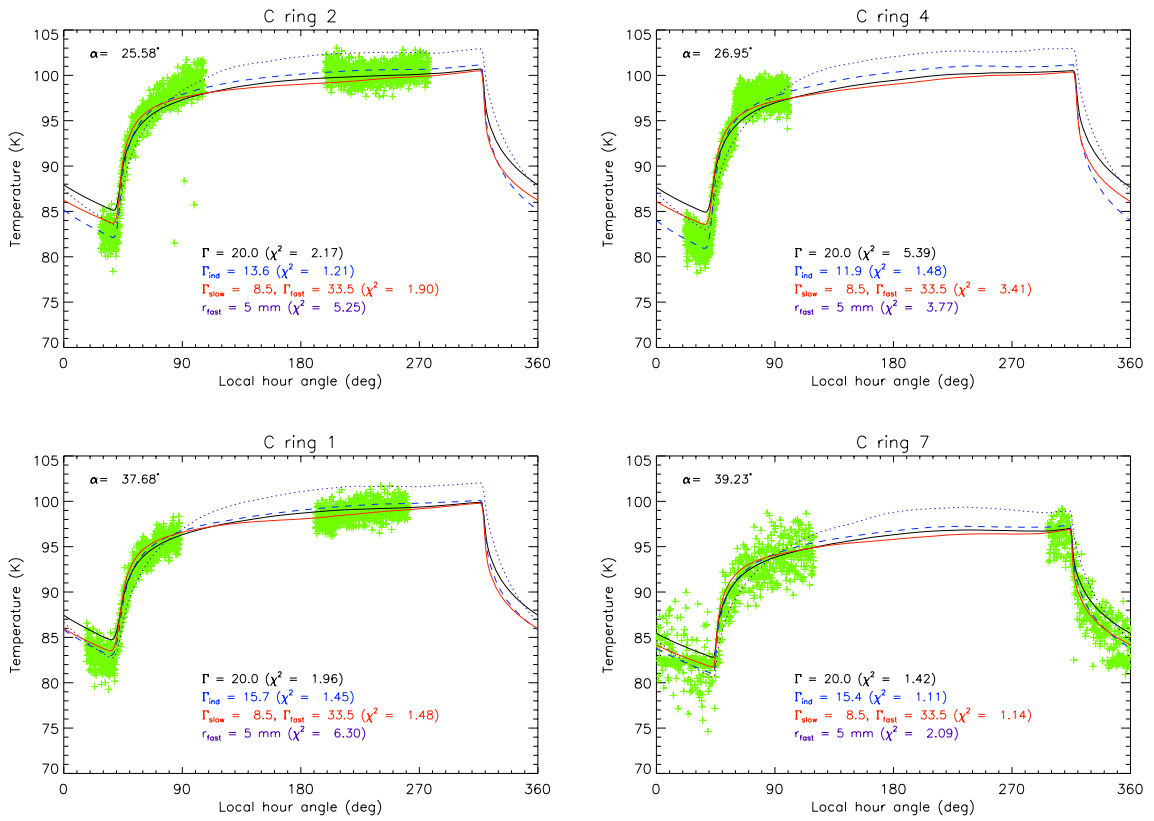


Fig. 1. Morishima et al.

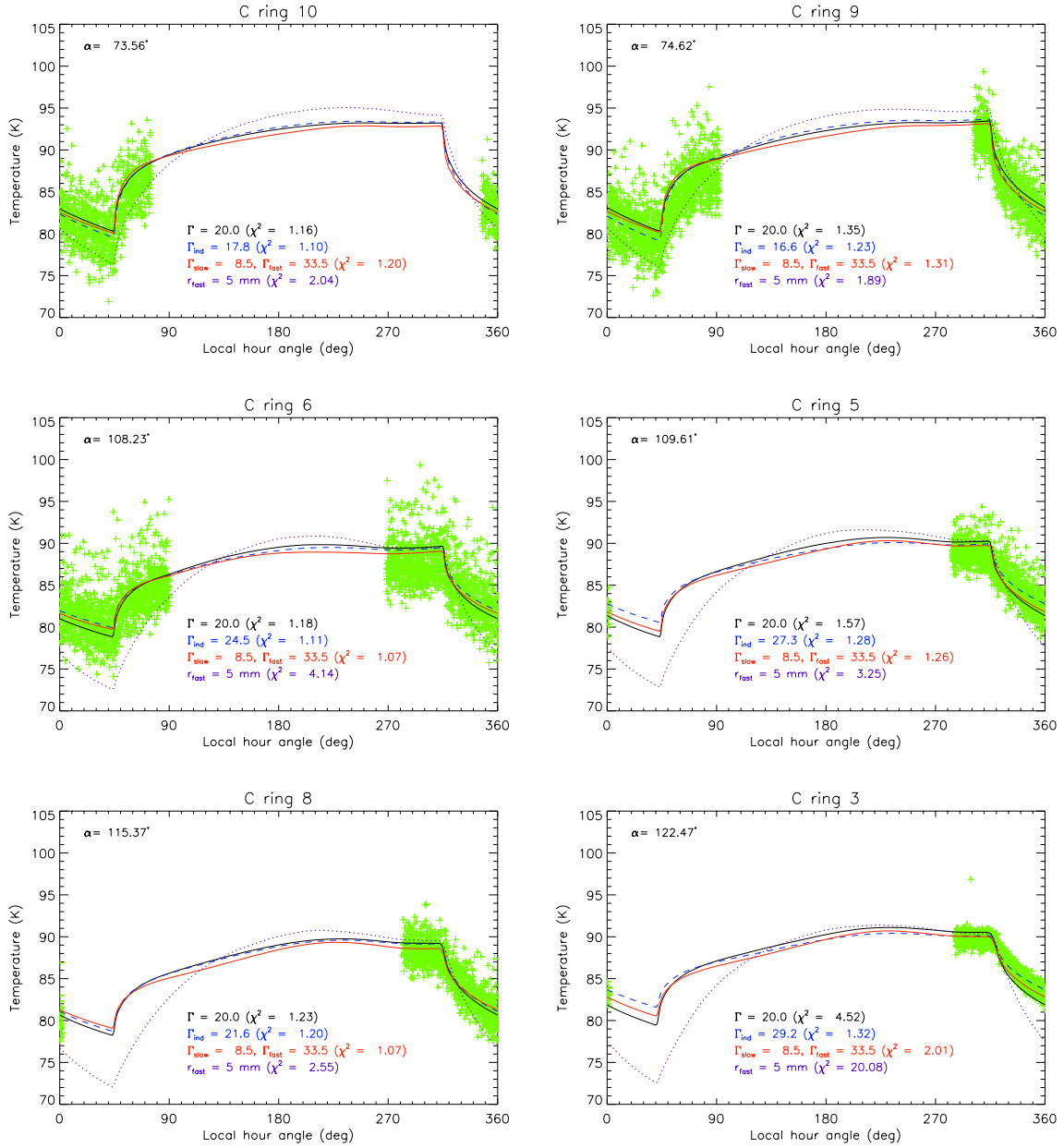


Fig. 1-continued.

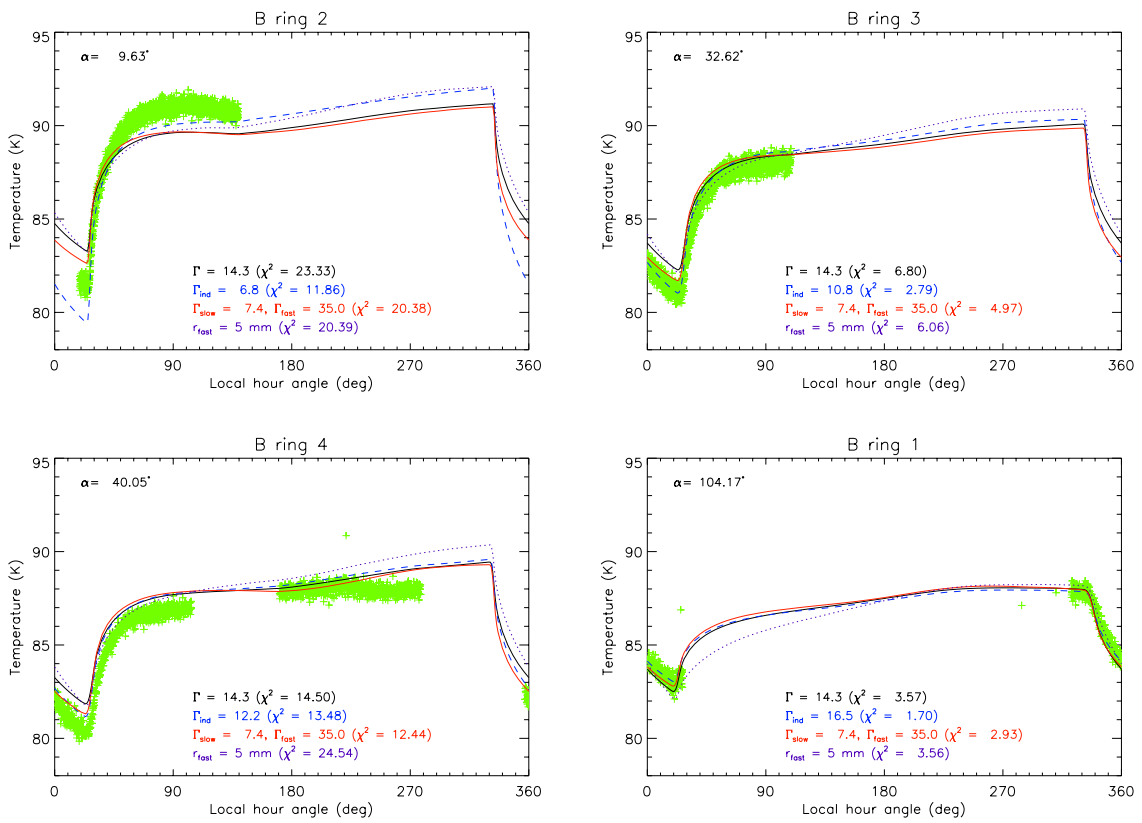


Fig. 2. Morishima et al.

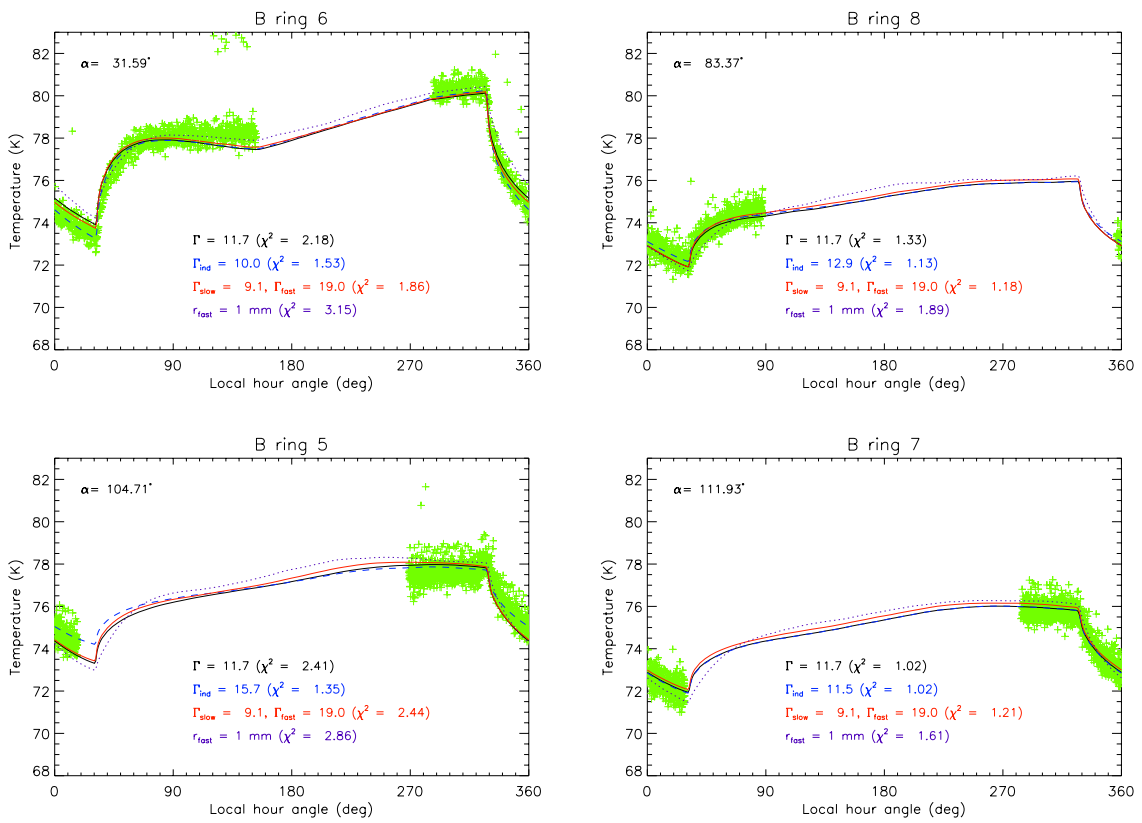


Fig. 2-continued.

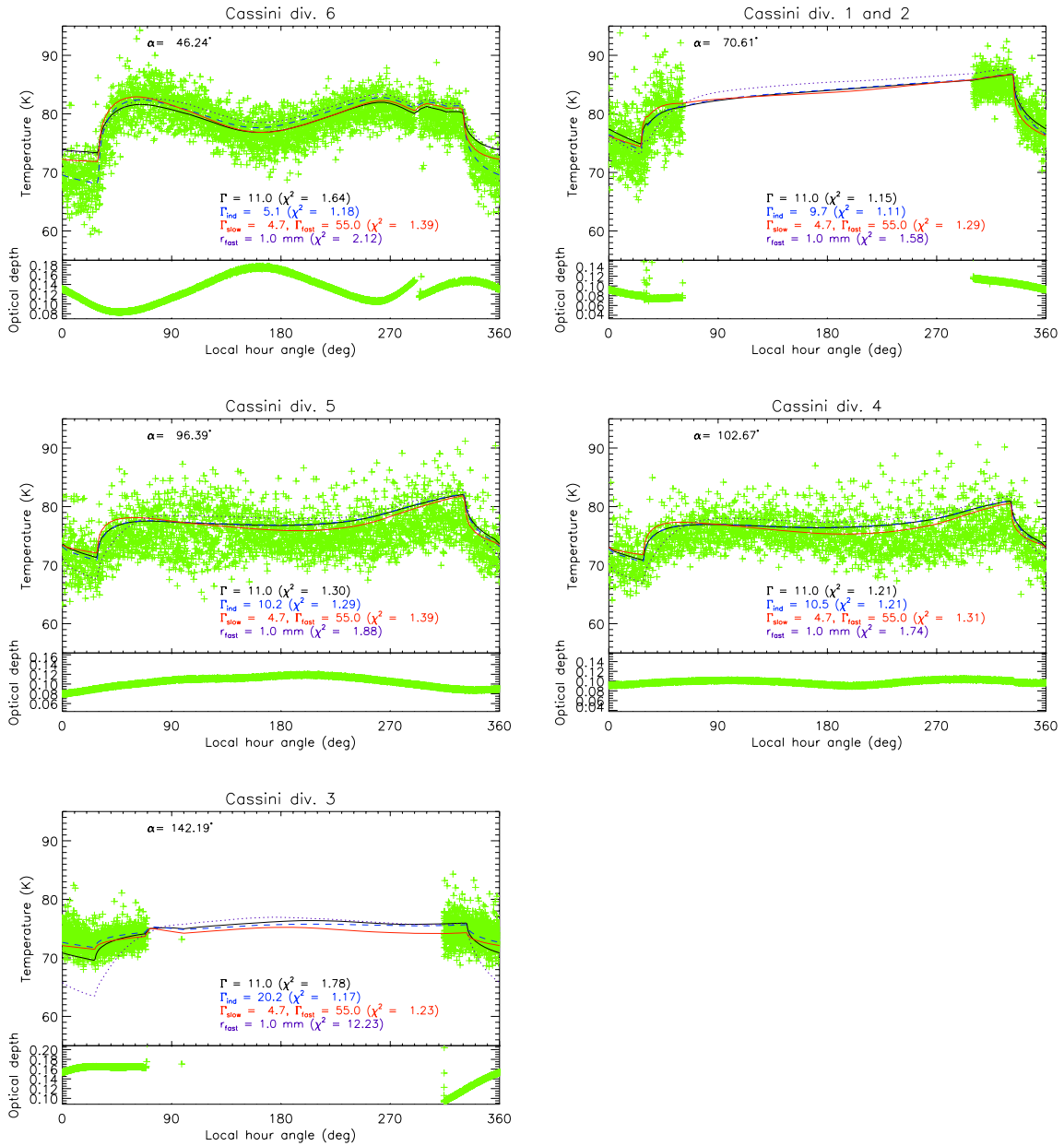


Fig. 3. Morishima et al.

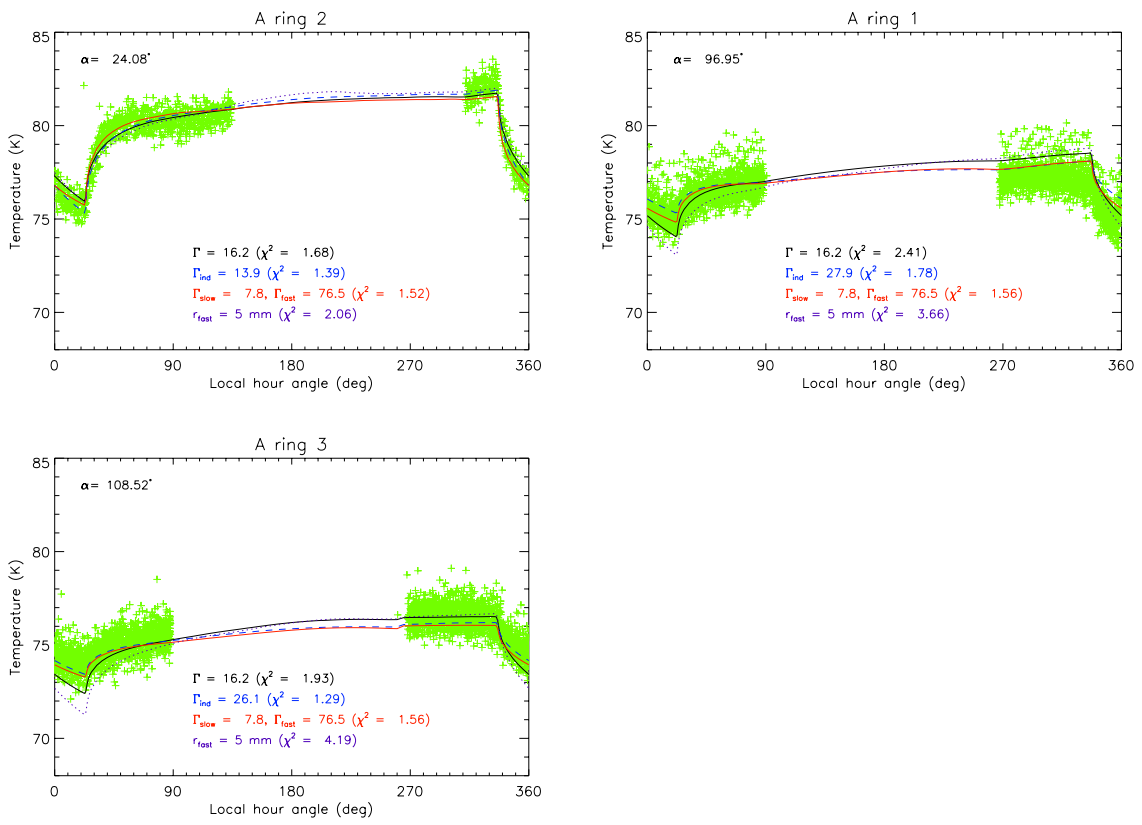


Fig. 4. Morishima et al.

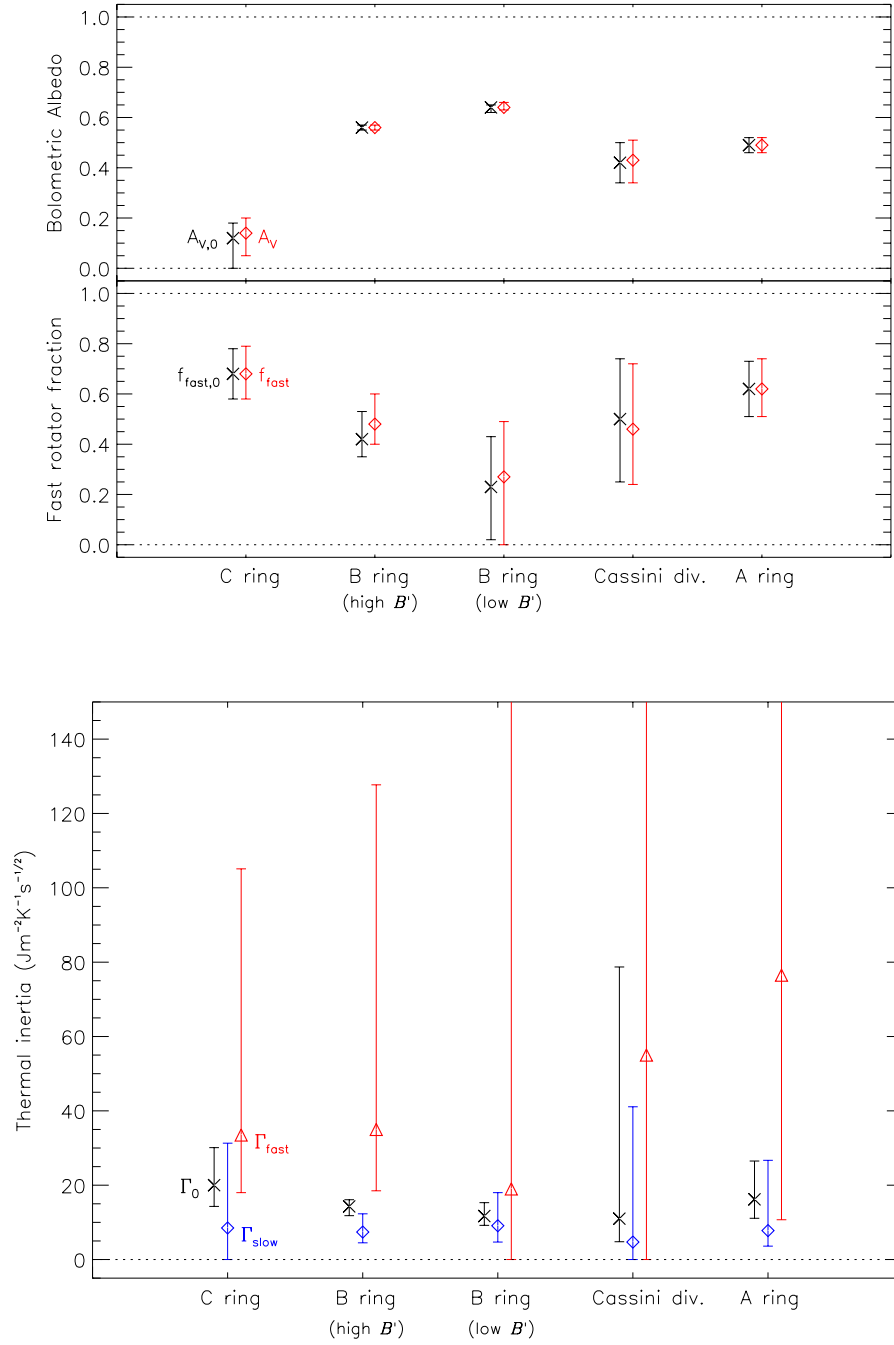


Fig. 5. Morishima et al.

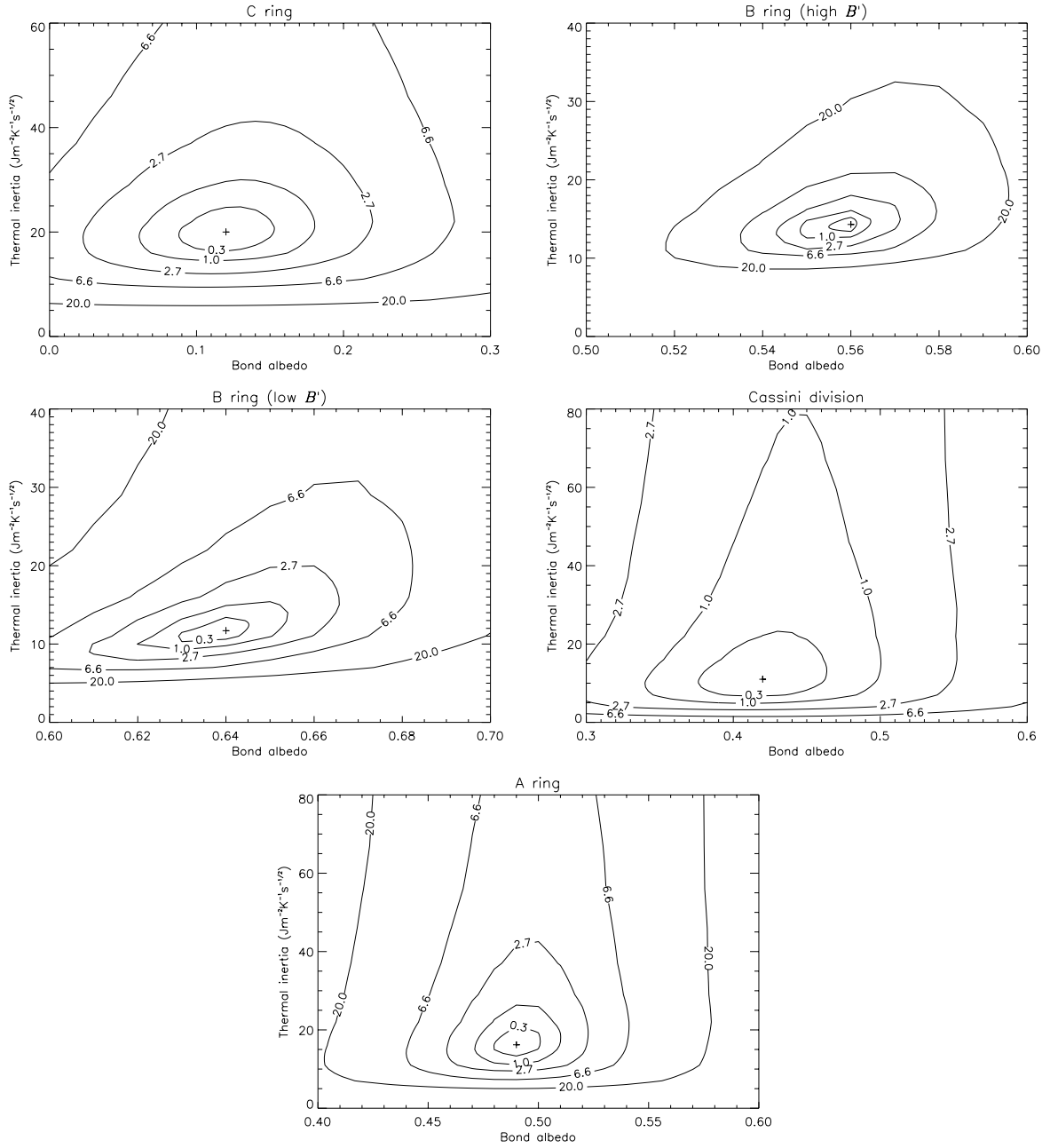


Fig. 6. Morishima et al.

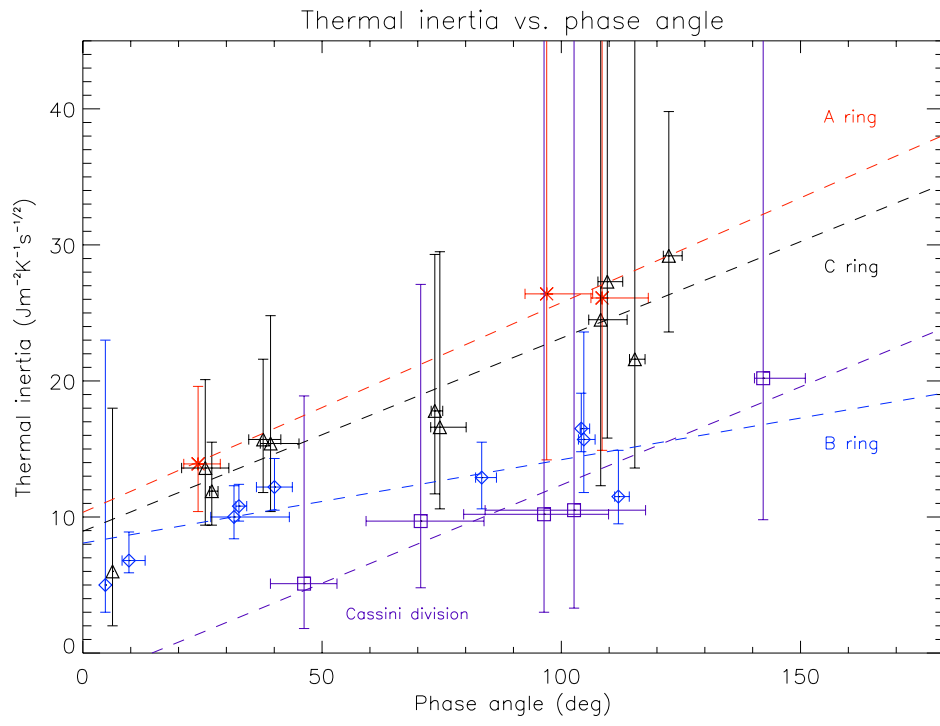


Fig. 7. Morishima et al.

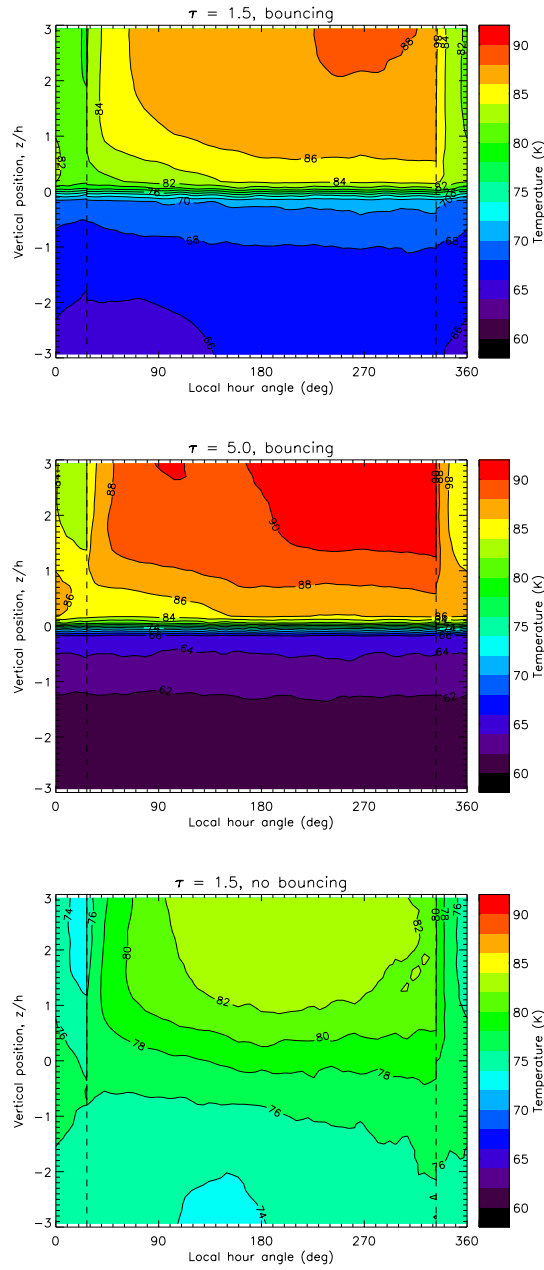


Fig. 8. Morishima et al.

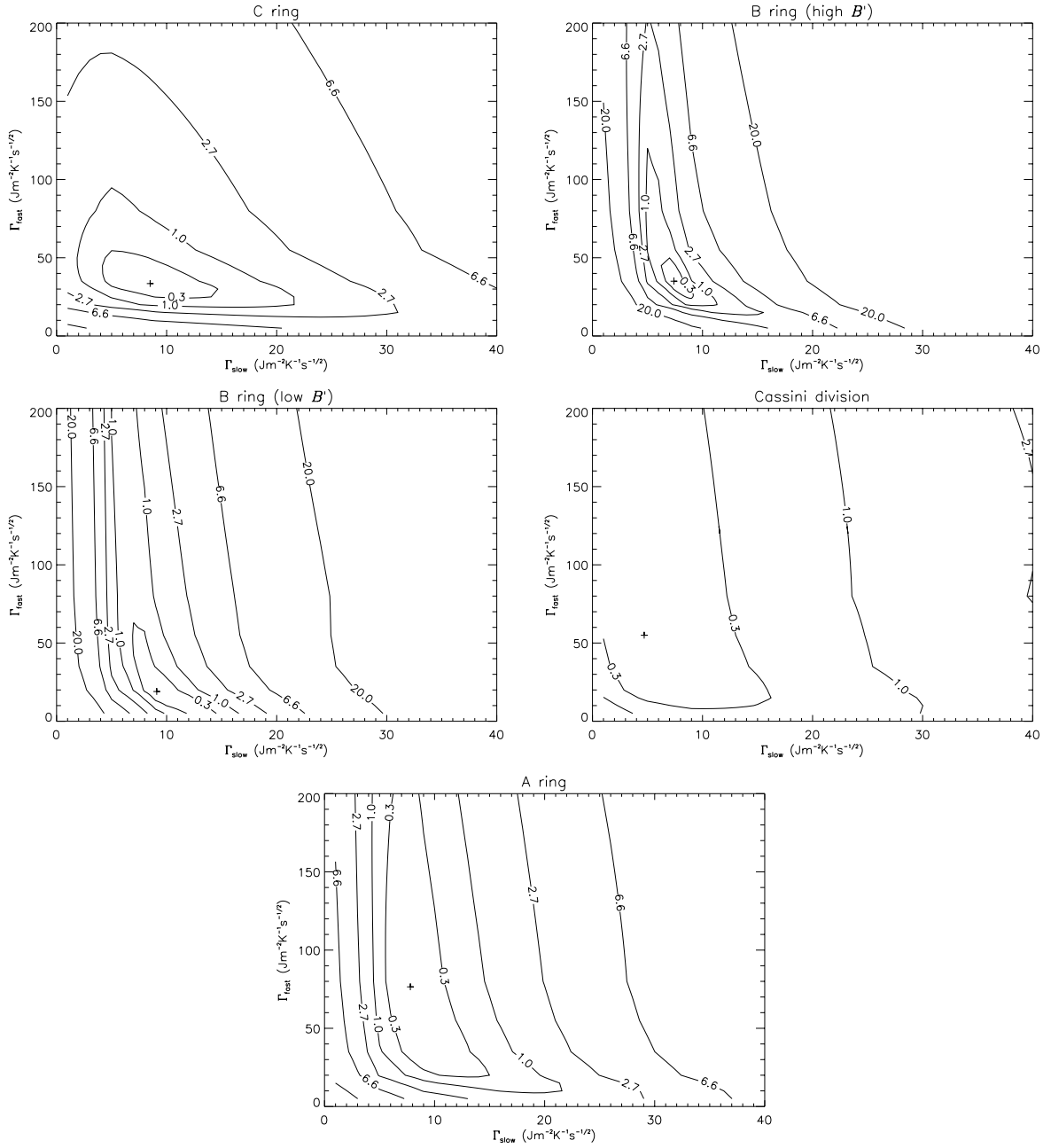


Fig. 9. Morishima et al.

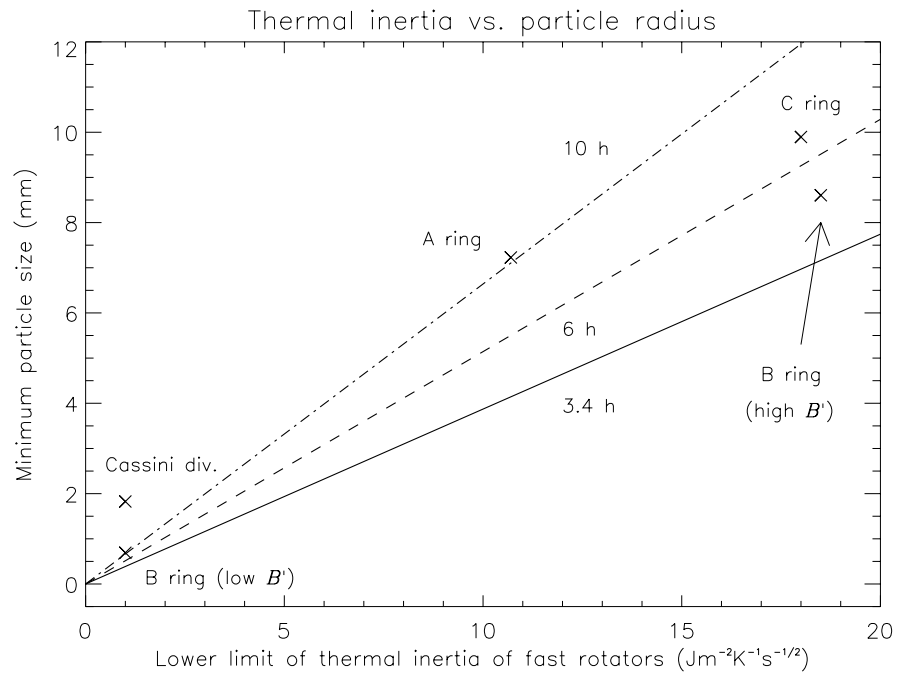


Fig. 10. Morishima et al.

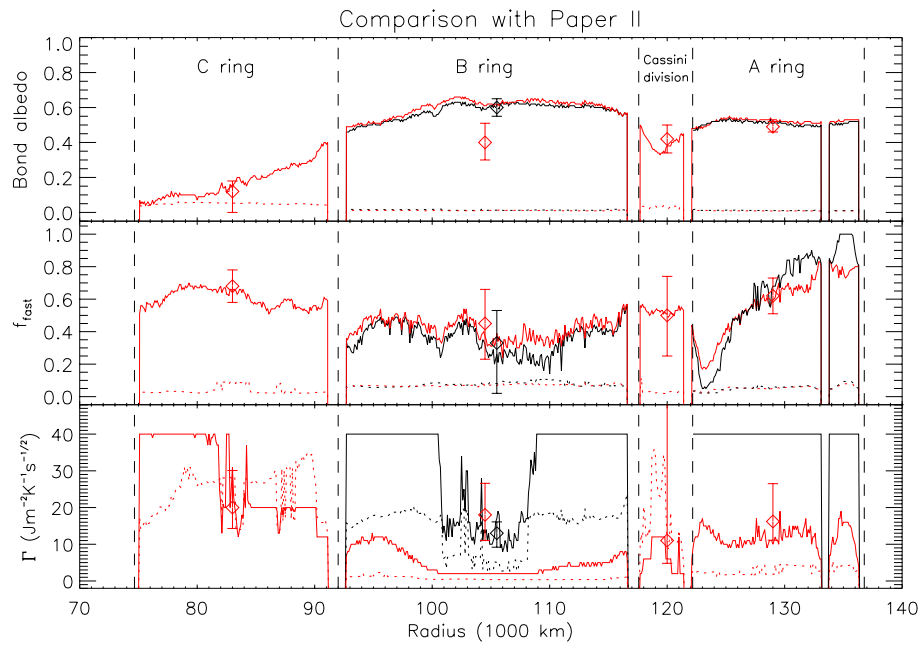


Fig. 11. Morishima et al.

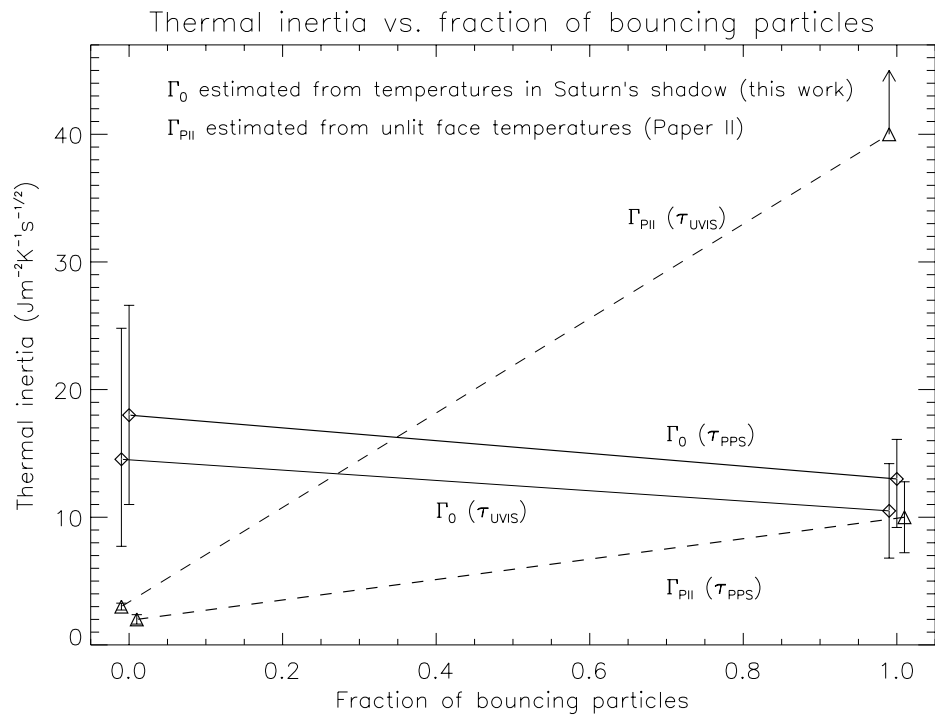


Fig. 12. Morishima et al.

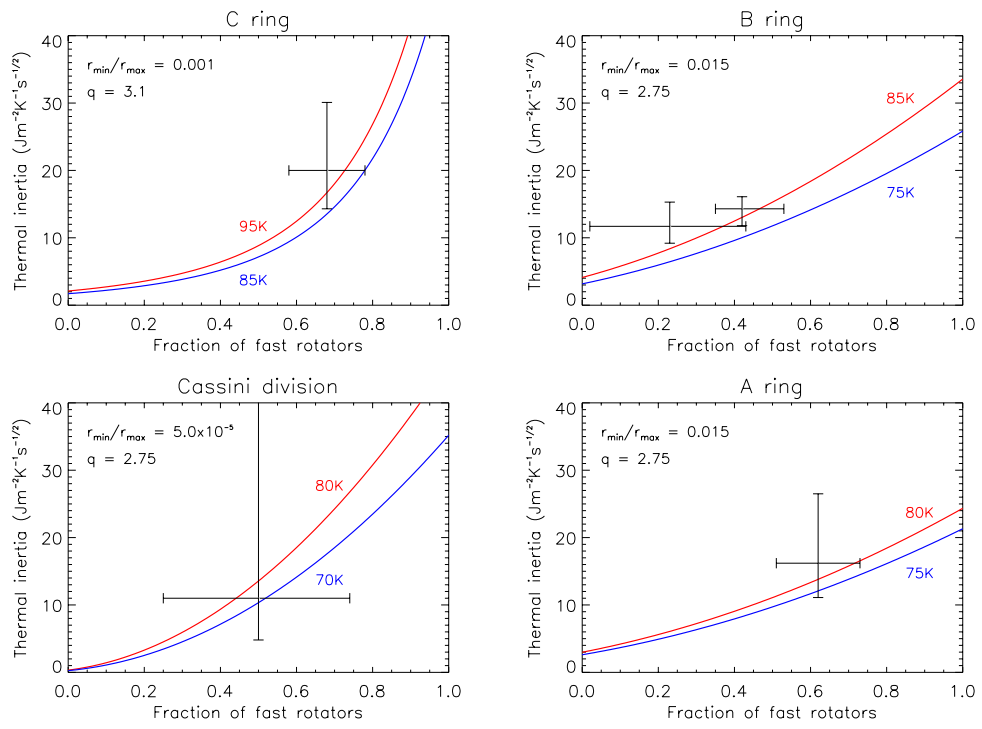


Fig. 13. Morishima et al.